Orographic Controls on Extreme Precipitation Associated with a Mei-Yu Front

IAN C. CORNEJO,[a] ANGELA K. ROWE,[a] KRISTEN L. RASMUSSEN,[b] AND JENNIFER C. DEHART[b]

[a] *University of Wisconsin–Madison, Madison, Wisconsin*
[b] *Colorado State University, Fort Collins, Colorado*

(Manuscript received 4 August 2023, in final form 11 December 2023, accepted 13 December 2023)

ABSTRACT: Taiwan regularly receives extreme rainfall due to seasonal mei-yu fronts that are modified by Taiwan's complex topography. One such case occurred between 1 and 3 June 2017 when a mei-yu front contributed to flooding and landslides from over 600 mm of rainfall in 12 h near the Taipei basin, and over 1500 mm of rainfall in 2 days near the Central Mountain Range (CMR). This mei-yu event is simulated using the Weather Research and Forecasting (WRF) Model with halved terrain as a sensitivity test to investigate the orographic mechanisms that modify the intensity, duration, and location of extreme rainfall. The reduction in WRF terrain height produced a decrease in rainfall duration and accumulation in northern Taiwan and a decrease in rainfall duration, intensity, and accumulation over the CMR. The reductions in northern Taiwan are linked to a weaker orographic barrier jet resulting from a lowered terrain height. The reductions in rainfall intensity and duration over the CMR are partially explained by a lack of orographic enhancements to mei-yu frontal convergence near the terrain. A prominent feature missing with the reduced terrain is a redirection of postfrontal westerly winds attributed to orographic deformation, i.e., the redirection of flow due to upstream topography. Orographically deforming winds converge with prefrontal flow to maintain the mei-yu front. In both regions, the decrease in mei-yu front propagation speed is linked to increased rainfall duration. These orographic features will be further explored using observations captured during the 2022 Prediction of Rainfall Extremes Campaign in the Pacific (PRECIP) field campaign.

SIGNIFICANCE STATEMENT: This study examines the impact of terrain on rainfall intensity, duration, and location. A mei-yu front, an East Asian weather front known for producing heavy, long-lasting rainfall, was simulated for an extreme rain event in Taiwan with mountain heights halved as a sensitivity test. Reducing terrain decreased rainfall duration in northern and central Taiwan. Decreases in rainfall duration for both regions is attributed to increased mei-yu front propagation speed. This increase in northern Taiwan is attributed to a weakened barrier jet, a low-level jet induced by flow blocked by the steep mountains of Taiwan. A unique finding of this work is a change in winds north of the front controlling movement of the front near the mountains in central Taiwan.

KEYWORDS: Asia; Complex terrain; Extreme events; Mei-yu fronts; Precipitation; Orographic effects

1. Introduction

Rainfall is a phenomenon almost ubiquitous across the world. The effects of a single rainfall event could be momentous, signaling the end of a drought or putting a stop to a wildfire. It can also be disastrous, creating flash floods or over watering crops. Complications of predicting such an event become exacerbated when rainfall occurs in complex topography. As rainfall scales from light to extreme, the danger and impact associated with such an event amplifies. Although rainfall accumulation can be viewed as an objective variable for determining extreme rainfall, it is actually rather contextual as a climatologically extreme event in one region might not be extreme in another.

One of the formative frameworks for characterizing extreme rainfall was proposed by Doswell et al. (1996) for improving flash flooding prediction in the United States. Precipitation P is expressed as

$$P = RD, \tag{1}$$

where R is the rainfall intensity and D is the duration of the rainfall. With these two variables, precipitation can be defined by scaling rainfall intensity and duration to create a spectrum of light to extreme rainfall with absolute magnitudes varying by climatic region. Deep convection often produces high-intensity, low-duration rainfall, whereas stratiform rainfall might populate the high-duration, low-intensity side of the spectrum. Tropical cyclones may lead to extreme rainfall through exhibiting both high intensity and duration. Mechanisms that enhance rainfall intensity are those that increase precipitation efficiency and vertical moisture flux. Rainfall duration can be enhanced by increasing the horizontal extent of a storm as well as decreasing the storm-relative speed. By characterizing individual events within this framework, an objective method can be used to improve our understanding of extreme rainfall formation, prediction, and impacts regardless of location.

While this framework can be applied to a range of rainfall events, it does not explicitly take into account topography's effect on rainfall intensity and duration. Topographic parameters such as terrain height, steepness, and geometry have complex relationships with not only rainfall intensity and duration, but rainfall location as well. Therefore, there is a necessity to incorporate topography into this framework. Prior work by Lin et al. (2001) suggests that terrain steepness is correlated with vertical ascent,

Corresponding author: Ian C. Cornejo, icornejo@wisc.edu

Publisher's Note: This article was revised on 10 July 2024 to correct the grant numbers listed in the Acknowledgments section.

DOI: 10.1175/MWR-D-23-0170.1

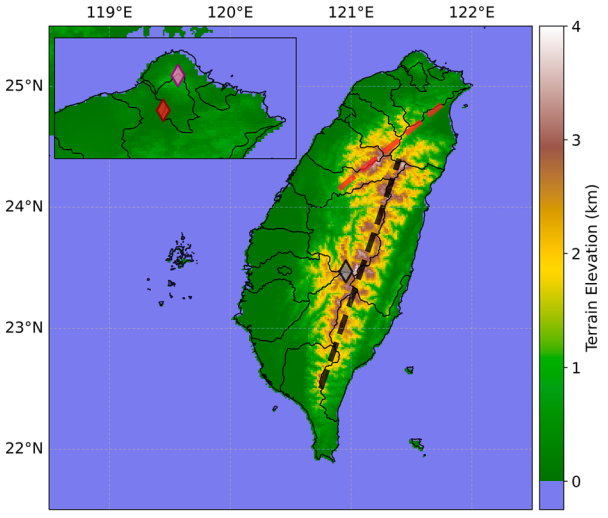

FIG. 1. Terrain elevation map of Taiwan with inset of northern Taiwan zoomed in. The dashed black line indicates the Central Mountain Range and the dashed red line indicates the Snow Mountain Range. The red marker indicates Taipei basin, the pink marker indicates the Yang-Ming Mountains, and the gray marker indicates Jade Mountain.

and thus leads to greater rainfall intensity. The limits of this theory and implications it has on rainfall duration has not yet been fully explored. The overarching goal of this research is to determine how topography modifies the intensity, duration, and location of mei-yu rainfall, which ultimately improves the ability to predict and forecast orographic precipitation.

An ideal location for studying extreme orographic precipitation is Taiwan, where steep topography makes up much of the island (Fig. 1). Taiwan frequently receives rainfall during the warm season, including the mei-yu season from mid-May to the end of June and the typhoon season from July to September (Henny et al. 2021). While the peak daily rainfall average has been found in the typhoon season, the 20-day running-average daily rainfall was found in the mei-yu season with a value of 12.5 mm day^{-1} over the entirety of Taiwan (Henny et al. 2021).

The mei-yu (known as the baiu/tsuyu in Japan and changma/jangma in Korea) signifies a transitional period of the waning wintertime northeast monsoon and strengthening summertime southwest monsoon (e.g., Chen 1983, 1992; Ninomiya 1984; Tao 1987). The southwest monsoon is relatively warm and transports moisture from the equator to the Bay of Bengal and then to Taiwan and the rest of East Asia (e.g., Chen 1993, 1994; Chang and Chen 1995; Yihui and Chan 2005). The monsoonal flow encountering Taiwan is typically southwesterly as a result. Opposite of the southwest monsoon is the northeast monsoon dominated by relatively drier and cold northeasterly flow originating from the Siberian high pressure system (e.g., Lau et al. 1988; Chen 1994; Jhun and Lee 2004; Yihui and Chan 2005). The boundary between these two monsoons forms the mei-yu front, a shallow, quasi-stationary front, along which convective systems are the predominant source of rainfall in Taiwan during the mei-yu season (e.g., Chen 1992; Cho and Chen 1995). The heaviest precipitation forms along the leading edge of the mei-yu front though slightly north of the wind shift line as the northward tilt of the front separates the rain from the convective updrafts (e.g., Chen 1992; Chen et al. 1998).

Rainfall intensity, duration, and location over land during the mei-yu season are influenced by Taiwan's topography (e.g., Li and Chen 1998; Yeh and Chen 2003; Davis and Lee 2012). Two major mountain ranges, the Zhongyang Range, or Central Mountain Range (CMR), which runs south-southwest to north-northeast (black dashed line in Fig. 1), and the Xueshan Range, also referred to as the Snow Mountain Range (SMR), which runs southwest to northeast (red dashed line in Fig. 1), cover roughly two-thirds of the entire island. The maximum terrain height on the island is found at Yushan, or Jade Mountain, with an altitude of 3952 m (gray marker in Fig. 1). Precipitation in the most densely populated region of Taiwan, Taipei basin (red marker in Fig. 1), is often heavily influenced by the nearby SMR and the Yang-Ming Mountains (pink marker in Fig. 1) (e.g., Tu et al. 2022).

With such complex topography and frequent heavy rainfall, Taiwan has hosted numerous field campaigns focusing on orographic precipitation during the mei-yu season, including the Taiwan Mesoscale Experiment (TAMEX) in 1987 (Kuo and Chen 1990) and the combined Terrain-influenced Monsoon Rainfall and Southwest Monsoon experiments (TiMREX/SoWMEX) in 2008 (Jou et al. 2011). Results from these campaigns, along with model-based work, have shown that one of the most common orographically induced mesoscale features during the mei-yu season is the barrier jet. While the blocking is most evident near sea level, surface friction raises the height of these jets near 1 km MSL (S.-J. Chen et al. 1998; Y.-L. Chen et al. 2022). These jets are most common in the prefrontal sector of mei-yu fronts as stably stratified southwesterly flow becomes orographically blocked by the CMR (Chen et al. 2022; Li and Chen 1998). The blocking creates a windward ridge, which induces a pressure gradient between northern and southern Taiwan causing a redirection of the prefrontal southwesterlies into southerlies. These southerlies converge with the mean flow to form the barrier jet in northwestern Taiwan (Chen et al. 1998; Yeh and Chen 2003). Since these jets are often found in the prefrontal sector, they can interact with the front. One example is through the barrier jet colliding with a cold pool ahead of a mei-yu front, slowing the progression of the front with rainfall implications for the densely populated regions of Taipei basin (e.g., Ke et al. 2019).

Another way in which orographic modification of the mei-yu front occurs is the splitting of the front upon approaching the SMR (Chen 1992). This splitting produces a windward front that resides west of the CMR and a leeside front that resides east of the CMR, each propagating south with the windward front being the most extreme from a rainfall perspective (Chen 1992). In a climatology from Wang et al. (2012), rainfall was found to be linked not only to front placement, but also topography. Frontal placement, however, was set at the western coastline in their study as it is difficult to pinpoint the mei-yu front on land near steep terrain. Therefore, how the fronts are modified by orography as they propagate south over land through the mountainous island is still an active research topic.

A mei-yu front case that produced extreme rainfall throughout Taiwan occurred 1–3 June 2017. This mei-yu front moved

TABLE 1. Parameterization schemes used in WRF Model.

Microphysics	Aerosol-aware Thompson microphysics (Thompson and Eidhammer 2014)
Longwave and shortwave radiation	Rapid Radiative Transfer Model for general circulation models (Iacono et al. 2008)
Surface layer	Monin–Obukhov surface layer scheme (Janić 2001)
Land surface interaction	Unified Noah land surface model (Tewari et al. 2004)
Boundary layer	Yonsei University boundary layer scheme (Hong et al. 2006)

onshore in northern Taiwan producing intense rainfall over Taipei Basin before propagating south into central Taiwan where rainfall persisted on the windward slopes of the CMR. Leading up to the start of the event, most of Taiwan's Central Weather Administration (CWA) front-associated extreme rainfall checklist criteria (Wang et al. 2012) were met, including a prefrontal low-level jet (Arakane et al. 2019; Chung et al. 2020; Tu et al. 2020, 2022; Wang et al. 2023). Arakane et al. (2019) noted a strengthening of both postfrontal and prefrontal wind speeds and enhanced low-level moisture transport to Taiwan linked to the influence of Tropical Cyclone Mora, which formed in the Bay of Bengal on 28 May 2017. The resulting enhanced frontal convergence and moisture transport within an enhanced marine boundary layer jet (Tu et al. 2020) contributed to an anomalously strong rainfall event for both northern and central Taiwan over a 2-day period. Questions remain, however, on the intensity and duration of rainfall along the front relative to the topography. Tu et al. (2022) began to explore this by modeling this event with a terrain sensitivity experiment removing only the northernmost Yang-Ming Mountains. What their study does not address is how sensitive frontal rainfall is to the larger topography of the CMR and SMR and how the terrain modifies the front when it progresses southward to central Taiwan.

This study will expand on prior research to better understand how orography modified the location, intensity, and duration of rainfall associated with the 1–3 June 2017 mei-yu front. To address this broader goal, the specific science objectives are to

1) Determine how the orography modified the mei-yu front, comparing the interactions in northern Taiwan with those less studied in central Taiwan.
2) Understand the impact of this frontal modification on rainfall intensity, duration, and location.
3) Compare orographically modified mechanisms leading to extreme rainfall in northern versus central Taiwan.

Section 2 will discuss the data and methods employed in this study to isolate topographic influences on rainfall during this extreme rainfall event. Section 3 will provide an overview of the rainfall associated with the 1–3 June 2017 mei-yu front case. Sections 4 and 5 describe the modification of the mei-yu front for both northern and central Taiwan, respectively. Section 6 will include conclusions of this study as well as plans to continue this work in the future.

2. Data and methods

a. Observational datasets

Observational radar datasets were provided by the CWA. The operational radar network of Taiwan consists of 12 radars: 4 S-band and 8 C-band radars. To track movement of the front close to Taiwan using radar reflectivity, data from the S-band Radar Code of Wu-Fenshan (RCWF) radar (25.07°N, 121.77°E) and Radar Code of Chigu (RCCG) radar (23.15°N, 120.09°E) were used. Raw RCWF and RCCG files were first converted into CfRadial format (Dixon and Lee 2016) using the Lidar Radar Open Software Environment—"Topaz" (Bell 2022). Once converted, the radar data was plotted using the Python ARM Radar Toolkit (Helmus and Collis 2016) to examine the evolution of precipitation throughout the event.

To quantify rainfall accumulation for the case, the Quantitative Precipitation Estimation and Segregation Using Multiple Sensors (QPESUMS) system was used. The QPESUMS system is a 10-min frequency rain gauge corrected rain rate and rainfall accumulation product produced by the CWA (Chang et al. 2021). The system integrates rain rates from the 12 operational radars to create a gridded rain rate product that is corrected using the 1000+ rain gauges on the island. The 1-h accumulation precipitation product with 0.0125° × 0.0125° resolution spanning 20°–27°N, 118°–123.5°E was used for its coverage and ability to quantify rainfall within rainbands associated with the mei-yu front. An accompanying terrain elevation dataset provided by CWA with similar resolution and horizontal extent as the 1-h accumulation QPESUMS product was used for topographical subdivision of rainfall accumulation.

b. Weather Research and Forecasting (WRF) Model

The WRF Model is a nonlinear, nonhydrostatic, full physics numerical weather prediction model developed by members of the National Science Foundation (NSF) National Center for Atmospheric Research (NCAR), National Weather Service, and the meteorological community. For this study, version 4.1.3 is used (Skamarock et al. 2019) with parameterization schemes listed in Table 1. These parameterization schemes were chosen to follow past modeling studies of the mei-yu front (Tu et al. 2022; Zhang et al. 2023; Zhao et al. 2023; Paul et al. 2021). The model was initially run with 40 ensemble members using two nested grids, each with 50 vertical levels, and an inner and outermost grid resolution of 3 and 9 km, respectively (Fig. 2). The methodology for modeling these 3- and 9-km nested grids follows that of Zhang et al. (2019). The model was initialized using model data from the Global Forecast System. These members were run from 1200 UTC 1 June to 1200 UTC 3 June 2017 with 12-h time steps for the outermost grid and 3-h time steps for the innermost grid.

The ensemble member that most resembled the observations for this event with regards to timing and accumulation of rainfall associated with the mei-yu front was selected for this analysis. The NDOWN program was used on that member to downscale a third, 1-way nested innermost grid with horizontal resolution of 1 km and 15-min output frequency (Fig. 2). To isolate the orographic influence on rainfall, the NDOWN program was repeated

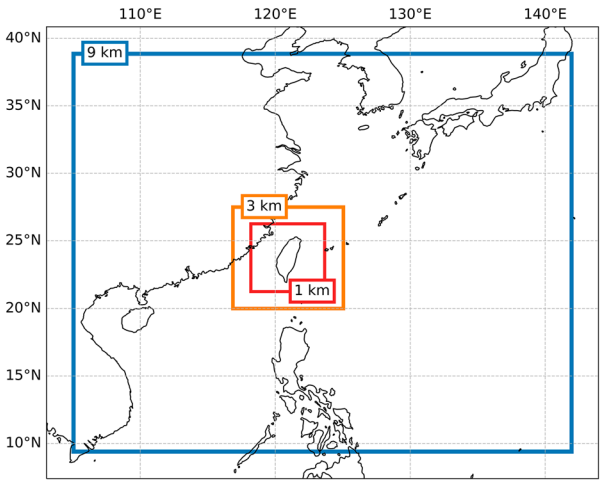

FIG. 2. Horizontal extent of the three WRF domains. The blue, orange, and red boxes represent the 9-, 3-, and 1-km grids, respectively.

using the same 1-km resolution and 15-min output frequency, but with halved terrain for the innermost grid only. The 3-km ensemble member used to force the 1-km runs has data extrapolated to sea level. Data gap "shocks" are dampened by interpolating this extrapolated data to match the sigma coordinates of the 1-km simulations as part of the model preprocessing steps. Additionally, to reduce any erroneous model spinup features, analysis of the model data begins 6 h after model initialization. The gradient in Taiwan's terrain height is large compared to much of the world with mountain peaks near 4-km height a short distance away from the coastline. By placing this event in a halved terrain environment, the results are more applicable to regions with more gradual and shallow topography. Since this study focuses on changes in rainfall associated with changes in topography and not the predictability of the event, only results from this innermost grid will be analyzed. These 1-km resolution model runs will hereafter be labeled Control and Half-T. All analysis of WRF data was conducted using MetPy (May et al. 2022) and WRF-Python (Ladwig 2017).

c. *Intensity and duration framework*

To translate the Doswell et al. (1996) intensity and duration framework into a methodology for categorizing extreme rainfall using the QPESUMS and WRF datasets, the following method was used:

1) For each QPESUMS and WRF grid point, build a time series of 1-h rainfall accumulation over the 42-h datasets.
2) Define rain periods within the 42-h period where minimum rainfall for any hour is at least 0.25 mm (i.e., minimal detectable rainfall by QPESUMS). To account for brief pauses in continuous rainfall at a grid point resulting from slight shifts in rainfall location, consecutive rain periods with gaps in rainfall of 1 h are combined into one rain period.
3) Each rain period at a grid point has a total accumulation of rainfall and a contiguous duration that are both used to define an average rain rate in millimeters per hour. The contiguous duration and average rain rate act as proxies for the duration and intensity ingredients introduced in Doswell et al. (1996).

The choice to allow for 1-h gaps was based on a comparison of four different methods of defining duration: noncontiguous duration where any time gap is allowed, contiguous duration with no gap allowance, contiguous duration with 1-h gap allowance, and contiguous duration with 2-h gap allowance. The 1-h gap allowance best fits the objectives of this study. Noncontiguous duration strongly diluted the maximum average rain rate achievable and resulted in too few rain periods. Noncontiguous duration is best served for studies where the source of rainfall is less important. Within a 42-h period, a location within the mountains may receive orographic precipitation, a break occurs, then receive mei-yu frontal rainfall. If using a noncontiguous duration, this location would only have one rain period with combined orographic and mei-yu rainfall durations and intensities without differentiating the two.

Contiguous duration with no gap allowance results in far too many rain periods that if this data are broken up into terrain height bins, the majority of rain periods favor low-duration, high-intensity rainfall. Mei-yu fronts often slowly and unpredictably move north and south which would lead to many rain periods even though the mei-yu front may not have moved more than the adjacent grid point. Contiguous duration with 2-h gap allowance begins to dilute high rain rate rain periods. The 2-h gap is also a long period of no rainfall at a location and begins to lose physical meaning. For example, if a rain period is found within a single convective cell, a 2-h gap in rainfall is more likely to be caused by a second source of rainfall rather than the original convective cell moving back over the same grid point. In viewing results using no gap allowance and 2-h gap allowance (not shown), any differences with the 1-h gap allowance were small and did not impact the conclusions of this study. For these reasons, the 1-h gap allowance strikes a balance between number of rain periods, physical meaning, and dilution of high rain rates. For the remainder of this study, all instances of duration and intensity will be in the context of contiguous 1-h gap allowed duration and average rain rate.

3. Rainfall accumulation, intensity, and duration

a. *Observations*

The rainband associated with the mei-yu front is seen along the northern coast of Taiwan at 0000 UTC 2 June 2017 (Fig. 3a). The associated rainband was quasi-zonal extending at least ±2° longitude from Taiwan. The leading edge of the rainband had reflectivity values as high as 60 dBZ indicative of heavy rainfall. Trailing behind the leading edge of the front was a broader stratiform region with reflectivity values around 30 dBZ. It took 6 h for the mei-yu front to pass Taipei and move south toward the CMR (Figs. 3b,c). The leading edge of the front was near zonal on the western coastline, but tilted southwest to northeast on the eastern coastline. This tilt lagged the front on the eastern coastline relative to the front on the western coastline, a trend that became more prominent as time progressed from 0300 to 0600 UTC. The trailing stratiform precipitation behind the leading edge of the mei-yu front decreased in area but persisted

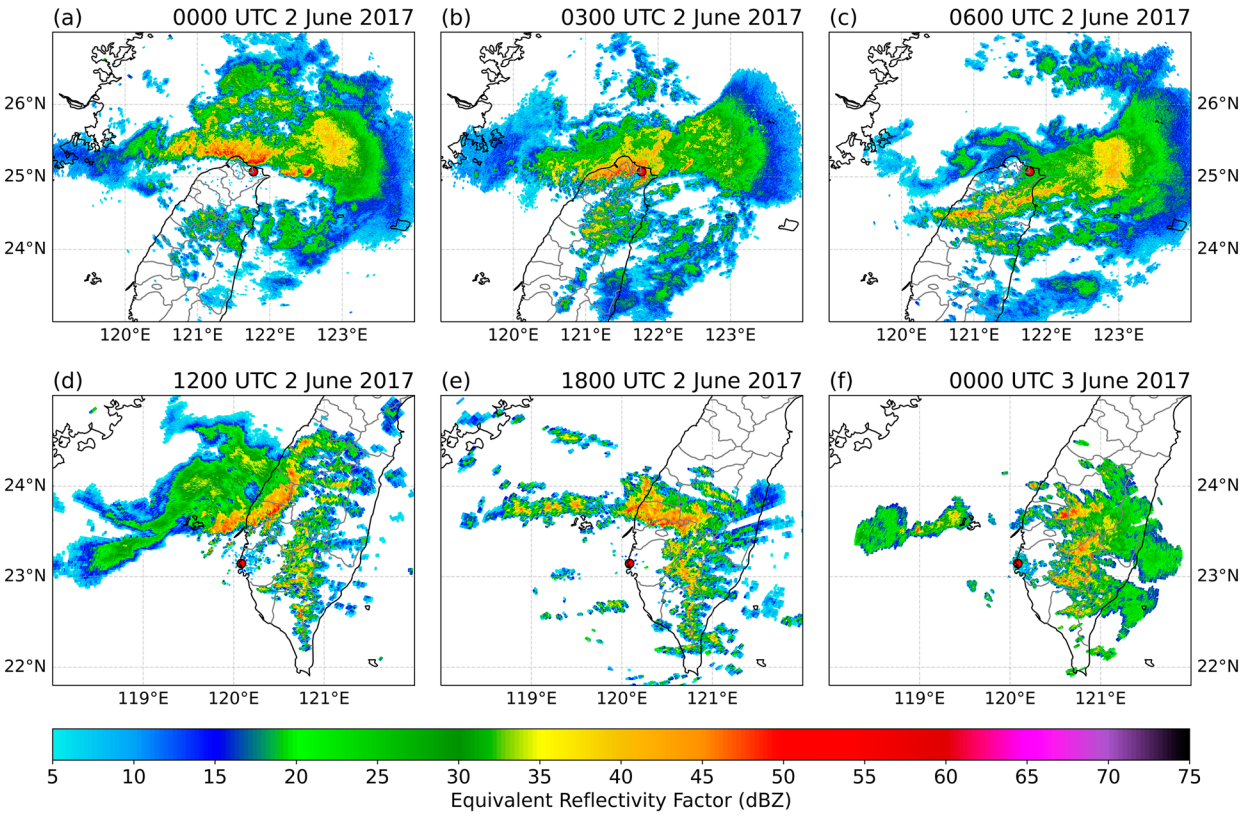

FIG. 3. Equivalent reflectivity factor (in dBZ) at (a) 0000 UTC 2 Jun, (b) 0300 UTC 2 Jun, (c) 0600 UTC 2 Jun, (d) 1200 UTC 2 Jun, (e) 1800 UTC 2 Jun, and (f) 0000 UTC 3 Jun 2017 using (a)–(c) RCWF at 0.5° elevation angle and (d)–(f) RCCG at 1.5° elevation angle. The red point indicates the location of the radar.

downstream and parallel to the tilted eastern leading edge of the eastern coastline.

At 1200 UTC 2 June 2017, the mei-yu rainband moved farther south (Fig. 3d). A more exaggerated north–south tilt in the leading edge was seen with the rainband not reaching into the higher terrain. Unlike 6 h prior, the trailing stratiform rainfall reappeared behind the leading edge of intense convection. Disconnected from the convection associated with the front, there were zonal bands of isolated convection along the windward slopes of the CMR that are indicative of rainfall produced by prefrontal flow impinging on steep topography. By 1800 UTC 2 June 2017, the rainband on the western coast returned to quasi-zonal orientation, but did not proceed further south relative to 6 h prior (Fig. 3e). Convection south of the rainband on the windward slopes continued. The front had become stationary with convection forming upstream in the South China Sea (SCS) and being advected downstream into the terrain. By 0000 UTC 3 June 2017, the rainband began to lose linear continuity with a short rainband extending from the high terrain to the coastline with a gap to another rainband off the coastline indicative of the end of the event and the regression of the front northward (Fig. 3f). Throughout this event, the front was characterized by periods of stationary positioning, most notably over central and northern Taiwan. Separate from the front, near constant rainfall was present on the western slopes of the CMR during this 2-day period.

The period of analysis for this study focuses on 1800 UTC 1 June to 1200 UTC 3 June 2017 to capture prefrontal periods, movement of the front over northern Taiwan, the quasi-stationary nature of the front over central Taiwan, and the northward receding of the front. To include the strong orographic precipitation not associated with the front, periods prior to and after the front is over Taiwan are included to fill out the intensity–duration spectrum in this case analysis. Within that 42-h period, maximum rainfall accumulation neared 1500 mm in the CMR (Fig. 4). This 42-h rainfall total would meet and exceed the 99th percentile of annual rainfall accumulation for much of the island (Tung et al. 2022). Bands of high precipitation are collocated with the initial approach of the front on the northern coastline and where the front became stationary in west central Taiwan. Although not associated with these bands, there are multiple regions with ≥500-mm rainfall on the windward slopes of the CMR hinting at the prominence of orographic precipitation induced by the monsoonal southwest flow not associated with the front.

b. WRF control

The Control run performed well in replicating rainfall distribution and timing during this event when compared to observations (Fig. 4). A key feature of this event, the mei-yu rainband extending off the west central coast, was well replicated in the WRF Model. The Control run did have a few differences from

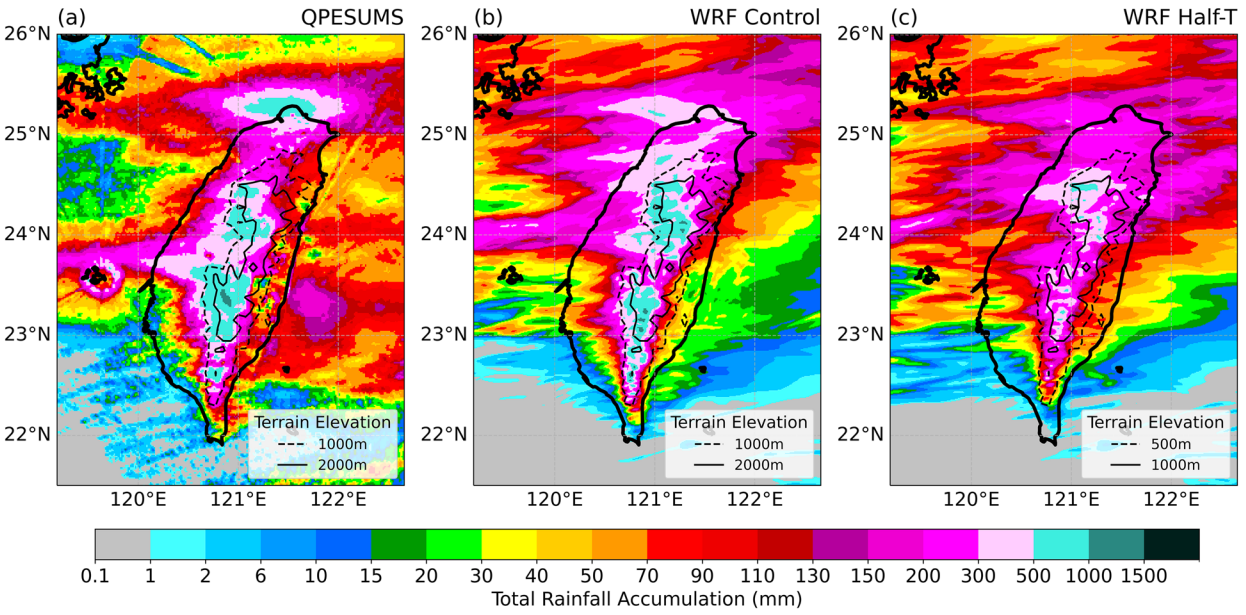

FIG. 4. Rainfall accumulation from 1800 UTC 1 Jun to 1200 UTC 3 Jun 2017 for (a) QPESUMS, (b) WRF Control, and (c) WRF Half-T.

QPESUMS, however. The rainband was shifted north approximately a quarter of a degree in latitude, the location of the rain maximum in northern Taiwan is moved farther inland, and the Control run lacks the heavier leeside precipitation east of the CMR.

To determine if the model replicated rainfall intensity and duration well, rain periods throughout the event are binned by terrain elevation and placed on a scatterplot of intensity and duration (Fig. 5). In comparing the lowest terrain bin (0–500 m), the Control run performs well in replicating the tapering intensity with increasing duration as well as a secondary maximum in intensity near 10.5-h duration (Figs. 5a,d). The Control run did not capture the low-duration, high-intensity rainfall found in QPESUMS. The medium terrain bin (500–2000 m) is also simulated well in Control with a decrease in low-duration, high-intensity rainfall and an increase in the intensity of maximum-duration rainfall (Figs. 5b,e). The high terrain bin (2000–4000 m) in QPESUMS has maxima in intensity around 21 and 42 h, while Control generally increases in intensity with increasing duration (Figs. 5c,f). That being said, an increase in density to higher durations with increasing height is well replicated by the model.

For each grid point, the rain period with the highest rainfall accumulation is placed on a color matrix and mapped out to create a bivariate choropleth of intensity and duration (Fig. 6). This approach allows for spatial context of rainfall intensity and duration not captured in the scatterplots. Northern Taiwan exhibits a wide range of rainfall durations between 0 and 21 h in both QPESUMS and the Control run, but the northeastern coastline in the Control run is higher in duration than QPESUMS with rainfall between 21 and 31.5 h. Higher intensities on the northwestern coastline are similar between QPESUMS and the Control run. In central Taiwan, the mei-yu rainband is associated with the highest intensities and increasing terrain height is associated with increased rainfall duration relative to lower terrain. Both characteristics are shared between QPESUMS and the Control run regardless of the positioning of the mei-yu rainband. Smaller details such as the low-duration rainfall in southern Taiwan and low-intensity rainfall on the leeside of the CMR is captured well by the model. With how well the Control run replicates QPESUMS with regard to rainfall intensity, duration, location, and accumulation, the Control run can be confidently used for isolating topographic influences on precipitation at a high resolution.

c. *WRF Half-T*

The decrease in terrain height in the Half-T run led to a broad decrease in precipitation in high terrain and northern Taiwan (Fig. 4). The maximum rainfall accumulation in the Control run was 1422 mm whereas the maximum in the Half-T run was 654 mm, both found above the 2-km terrain height (1-km terrain height for Half-T). Median rainfall accumulation over Taiwan was 207 mm for the Control run while the median for Half-T was 164 mm. Much of southern and eastern Taiwan experience similar rainfall totals in both the Control and Half-T runs for elevations below 1 km for Control and 0.5 km for Half-T. A local maximum in rainfall accumulation is found in northwestern Taiwan in the Control run that is not present in the Half-T run. Additionally, the mei-yu rainband off the western coast has also shifted north in the Half-T run with a leeside band of precipitation that does not occur in the Control run.

In comparing WRF Control and Half-T through the intensity and duration framework, elevation bins were scaled to represent the same areas rather than the same elevations (Figs. 5d–i). For example, the low elevation bin for the Control run represents 0–500-m terrain height whereas the low elevation bin for the Half-T run represents 0–250-m terrain height. The reduction in terrain height had little effect on low-duration rainfall in the low elevation terrain bin but decreased the maximum rainfall

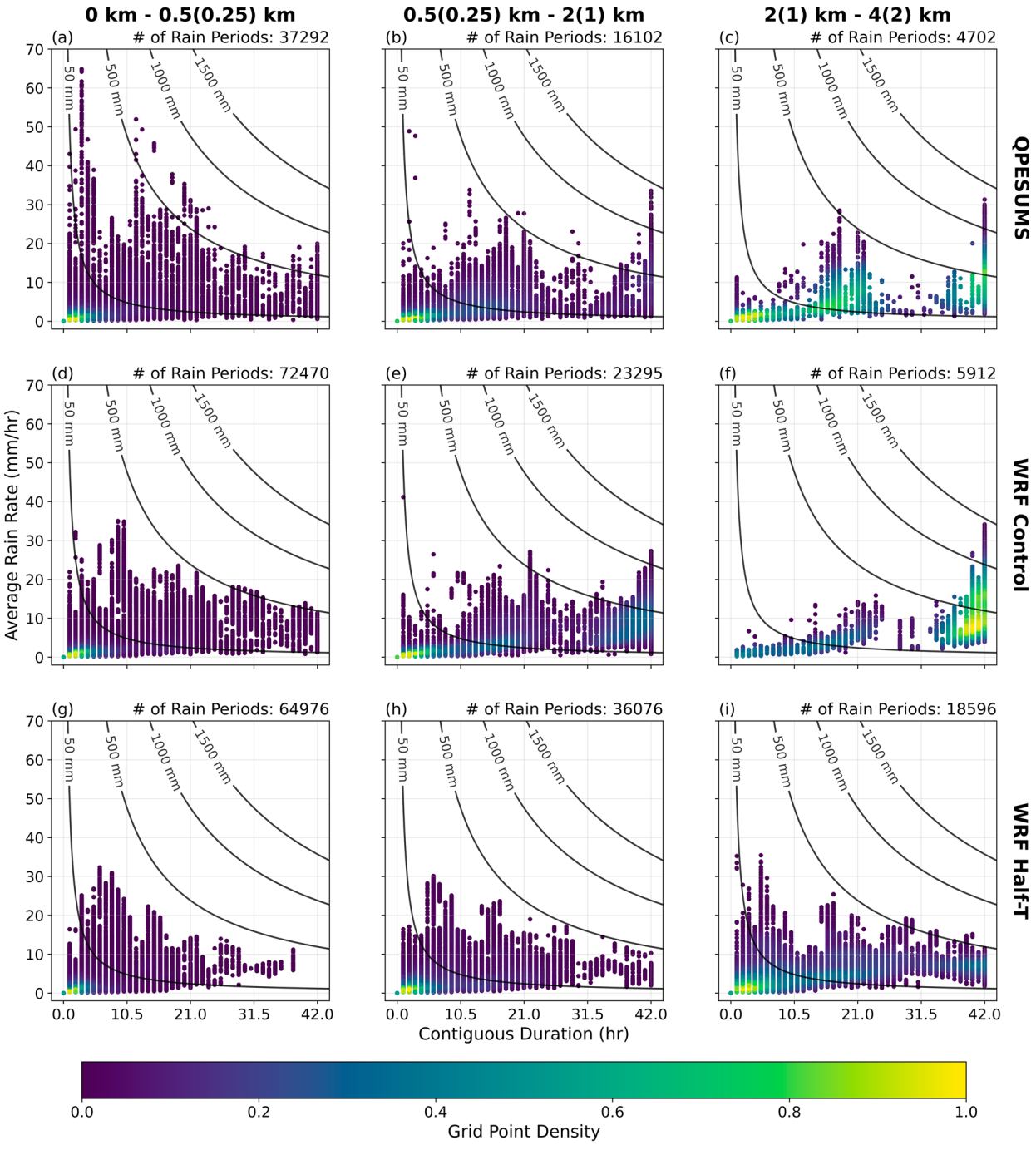

FIG. 5. Intensity and duration scatterplots for all (a)–(c) QPESUMS, (d)–(f) WRF Control, and (g)–(i) WRF Half-T rain periods over land (a),(d),(g) between 0- and 0.5-km (0–0.25-km); (b),(e),(h) between 0.5- and 2-km (0.25–1-km); and between 2- and 4-km (1–2-km) terrain height for WRF Control (WRF Half-T) using contiguous duration with 1-h gap allowance in rainfall between 1800 UTC 1 Jun and 1200 UTC 3 Jun 2017. Gray contours represent lines of constant rainfall accumulation (in mm).

duration from 42 to 38 h (Figs. 5d,g). Within the medium terrain height bin, few Half-T rain periods are able to attain a maximum rainfall duration of 42 h (Fig. 5h), and those that do are all low intensity with an average rain rate below 10 mm h^{-1} compared to 20 mm h^{-1} in the Control run (Fig. 5e). Within the highest elevation bin, the distributions of rainfall intensity and duration are most dissimilar (Figs. 5f,i). The Control run continues the shift in density toward high-duration rainfall as well as an increase in rainfall intensity at maximum rainfall duration. The Half-T run continues to have low intensity at high duration and

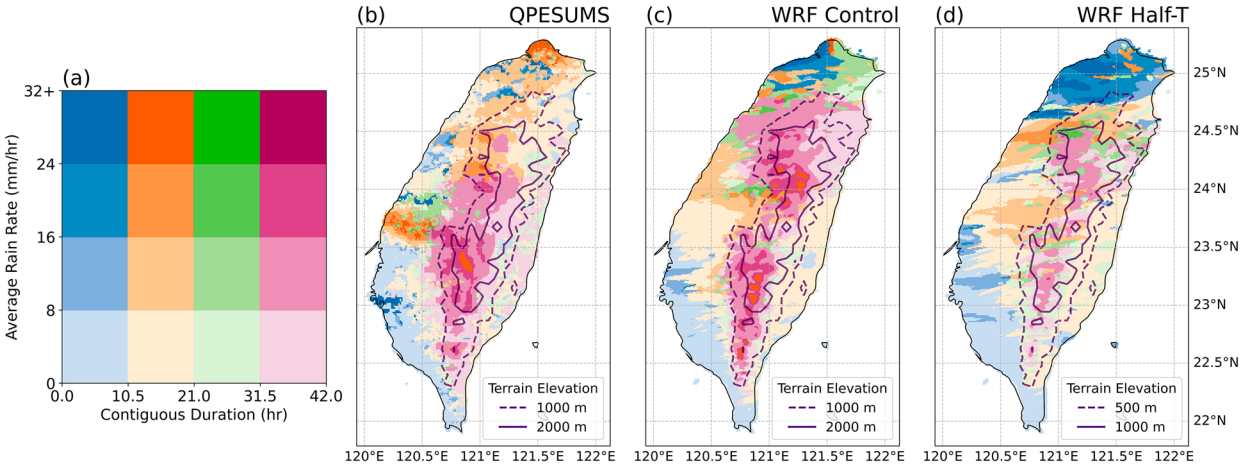

FIG. 6. Bivariate choropleth of contiguous duration and average rain rate of the highest-rainfall-accumulating period for each grid point using (a) the reference color matrix for (b) QPESUMS, (c) WRF Control, and (d) WRF Half-T.

higher intensity at low duration. The Half-T run also has a slight shift toward higher-duration rainfall, indicating that regardless of model run, areas of increased terrain height are likely to experience greater rainfall duration. Rainfall intensity does not increase with terrain height except in the case of maximum-duration rain periods in the Control run.

When mapped using the bivariate choropleth (Figs. 6c,d), spatial trends emerge to bolster the results of the intensity and duration scatterplots. At high altitudes found within the CMR, rainfall intensity decreases in the Half-T run. Within the Control run, much of the western sides of the CMR and SMR are within the 31.5–42-h rainfall duration bin, but the Half-T run drops to durations between 10.5 and 31.5 h. The most striking drop in intensity and duration can be found where the mei-yu rainband becomes quasi-stationary in the Control run. Within central Taiwan (23.5°–24.25°N), some of the most intense and highest duration rainfall is found within the Control run. However, in the Half-T run, a stark decrease in intensity from the western coastline to the CMR and a drop in rainfall duration above the 500 m terrain height contour highlights a region of interest for further analysis. Another region of interest for investigating orographic controls on rainfall intensity and duration is northern Taiwan (>24.75°N). Where the Control run has a wide array of low and high durations and intensities in northern Taiwan, the Half-T run experiences overall lower duration with similar intensities. Understanding the link between reduced terrain and the notable reductions in rainfall duration in these regions, northern and central Taiwan, will be the focus of the next two sections.

4. Northern Taiwan

a. *Barrier jet formation*

Prior work by Tu et al. (2022) highlights the sensitivity of the 1–3 June 2017 mei-yu front propagation to slight modifications in topography with the removal of the Yang-Ming Mountains in northern Taiwan. Their study found that the removal of those mountains increases the propagation speed of the front and also placed the barrier jet as a key contributor to lifting and heavy rainfall along the front. The sensitivity of the barrier jet and subsequent frontal rainfall by the CMR has not yet been explored, however. The barrier jet in their study was replicated well at 900 hPa within WRF in both the Control and Half-T run (Fig. 7). At 1800 UTC 1 June 2017, the Control run exhibits 900-hPa wind speeds above 50 kt (1 kt $\approx$ 0.51 m s^{-1}) along the northwestern coastline whereas the Half-T run is slightly weaker between 40 and 45 kt. Evidence of the barrier jet in both runs originating from upstream orographic blocking is found in southern Taiwan with southwesterly flow slowing down on approach toward the CMR. The degree of slowdown is larger for the Control run with flow off the coast between 30 and 35 kt and dropping to 10 kt near the CMR in the Control run while the Half-T run drops to 20 kt. High perturbation heights are found to be collocated with the slowdown of the flow (Fig. 7) for both the Control and Half-T run at 1800 UTC 1 June 2017. However, the Control run has a 5–10-m-greater height perturbation, giving confidence that orographic blocking is stronger in the Control run (Pierrehumbert 1984).

To diagnose the degree of orographic blocking, the Froude number is applied, defined as

$$\mathrm{Fr} = \frac{U}{Nh}, \tag{2}$$

where U is the wind speed orthogonal to a mountain, N is the Brunt–Väisälä frequency, and h is the mountain height. Froude number values larger than 1 are unblocked, allowing for orographic lifting of a parcel. For Froude numbers less than 1, a parcel's inertia is not able to overcome the atmosphere's stability, pushing orographic lift upstream of the orography. A portion of this flow orographically deforms, i.e., becomes redirected due to upstream topography (Pierrehumbert 1984; Kirshbaum et al. 2018; Chen and Lin 2005; Chen et al. 2008; Reinecke and Durran 2008). An orographic deformation radius can be defined as

$$L_d = \frac{Nh}{f}, \tag{3}$$

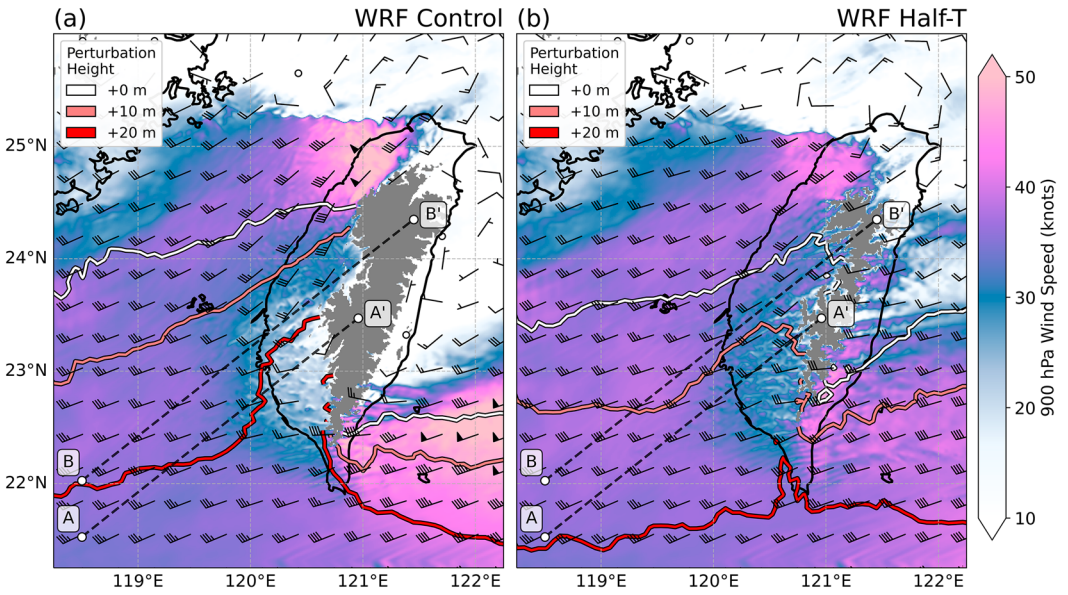

FIG. 7. The 900-hPa wind speed and wind barbs for (a) WRF Control and (b) WRF Half-T at 1800 UTC 1 Jun 2017. Contours represent positive 900-hPa perturbation heights. Cross sections are taken along lines AA′ and BB′.

where N is the Brunt–Väisälä frequency, h is the mountain height, and f is the Coriolis parameter (Pierrehumbert and Wyman 1985). In the presence of orographic blocking due to a mesoscale mountain range, the orographic deformation radius is the distance upstream of the orography whereby orographic deformation extends. For an idealized mountain range with length L_y, the orographic deformation radius becomes equal to L_y if the mountain range length is far less than that of the orographic deformation radius. The Froude number and orographic deformation radius in tandem can determine the degree and extent of orographic blocking. For example, for a Froude number less than 4/3, deceleration is found within the orographic deformation radius, and for a Froude number less than 2/3, zones of near stagnant air will also exist within the orographic deformation radius. Lin (1993) provides approximate measurements for Taiwan that can that be used for estimating the orographic deformation radius, with length of the CMR being approximately 300 km and the average height being 2 km. Assuming the Brunt–Väisälä frequency to be 0.01 s^{-1} and the Coriolis parameter is approximately 6×10^{-5} s^{-1}, the orographic deformation radius for Taiwan is approximately 333 km, slightly larger than the length of the CMR. With halved terrain height, the Half-T run will have an orographic deformation radius of 166.5 km, significantly less than the length of the CMR. For this reason alone, regardless of flow speed, differences in the orographic blocking extent should differ between model runs.

The extent and depth of the orographic blocking is analyzed through the cross sections as shown in Fig. 7. Cross section AA′ points from far off the coast inland to the peak of Jade Mountain. Cross section BB′ runs parallel to AA′ but is shifted north ending at the northernmost peak of the CMR to capture downstream effects of the orographic blocking. A modification to the Froude number is made to integrate the horizontal and vertical extent of orographic blocking along these cross sections such that it takes on a height-relative form (Viale et al. 2013; Riley Dellaripa et al. 2020; Marín et al. 2021):

$$\mathrm{Fr}(z) = \frac{U(z)}{N(z)(h - z)}. \tag{4}$$

Figures 8 and 9 show an along-cross-section wind speed that points toward the orography, a cross section-relative orthogonal wind speed, and a height-relative Froude number using the peak terrain height of the cross section and the along-cross-section wind speed. The cross section Froude number reveals if orographic blocking occurs, how far upstream from orography the blocking occurs, and how high blocking occurs. Therefore, this cross section approach, rather than a single point Froude number, allows for determination of the spatial extent of orographic blocking. For both AA′ and BB′ in the Control run, orographic blocking runs nearly the full extent of the cross sections with Froude number values under 1 below 2-km height (Figs. 8a,b). The lowest Froude numbers in each cross section are collocated with stagnant zones with near-zero along-cross-section wind flow situated near the terrain (Figs. 8c,d). Along-cross-section wind speeds below the 2-km blocking height slowdown when crossing the coastline for both AA′ and BB′, but for AA′ this slow down is greater in magnitude. A partial reason why is found in the orthogonal wind speeds (Figs. 8e,f). Off shore orthogonal winds go into the cross section for AA′ and BB′, but become near zero on shore for AA′ and stronger into the cross section for BB′, indicating that flow has turned counterclockwise relative to AA′ on land. Along-cross-section flow along AA′ is being orographically blocked and diverted to northern Taiwan as evidenced by the southerly flow found in BB′ in the Control run.

Within the Half-T run, orographic blocking is reduced along AA′ and BB′ (Figs. 9a,b). The only regions with Froude number less than 1 along AA′ are found within 10 km of the

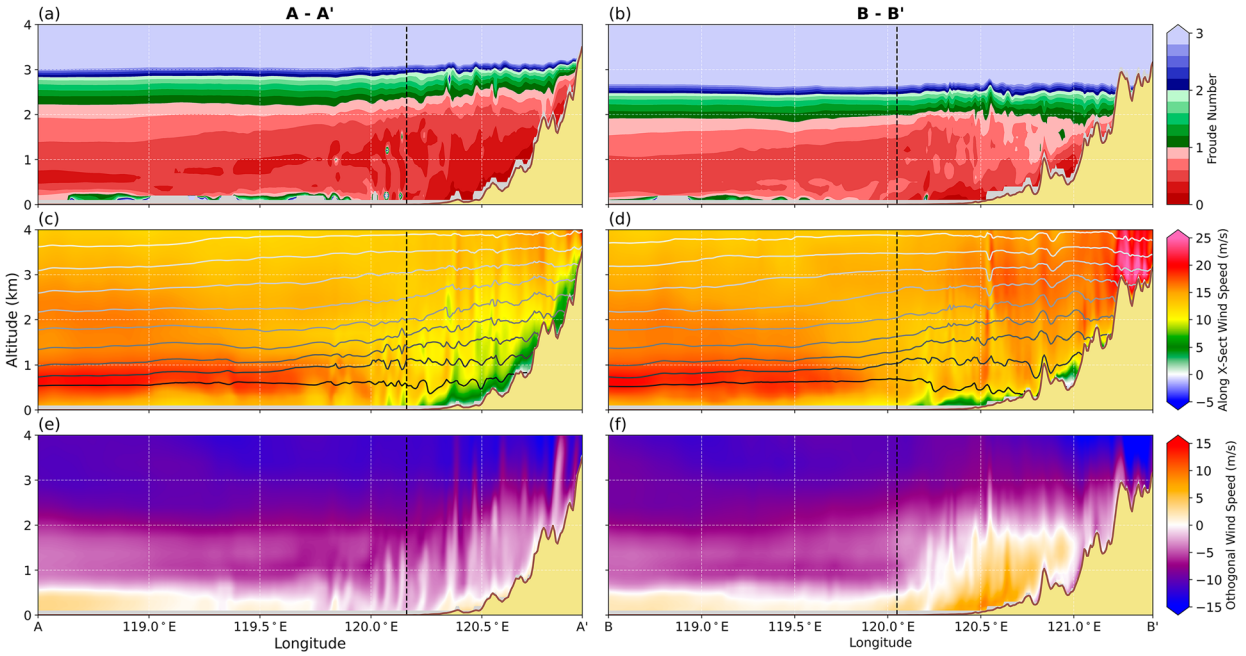

FIG. 8. Cross sections (a),(c),(e) AA′ and (b),(d),(f) BB′ at 1800 UTC 1 Jun 2017 of (a),(b) altitude-relative Froude number; (c),(d) along-cross-section wind speed and dry isentropes; and (e),(f) orthogonal wind speed for WRF Control. The black dashed line indicates the coastline.

topography. There is a corresponding slowdown of along-cross-section flow on land in AA′ (Fig. 9c) similar to the Control run (Fig. 8c) with near stagnant zones collocated with Froude numbers less than 1; overall, however, the along-cross-section winds are stronger below 2-km height in the Half-T run compared to the Control run. Orthogonal winds in Half-T running along AA′ (Fig. 9e) are similar in strength and direction to those found in the Control run (Fig. 8e). The result of this weaker orographic blocking in the Half-T run is seen downstream along BB′ where the positive orthogonal winds near the terrain (Fig. 9f)

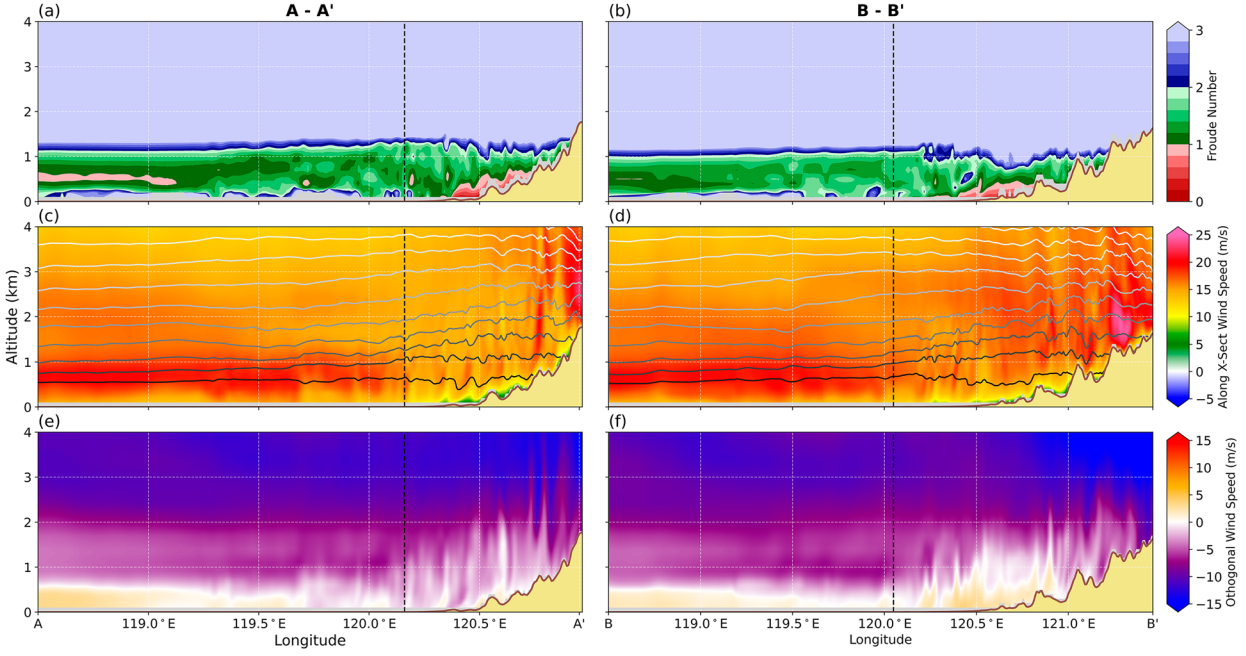

FIG. 9. As in Fig. 8, but for WRF Half-T.

are significantly weaker relative to BB′ in the Control run (Fig. 8f). Therefore, as southwest flow encounters Jade Mountain, the reduced terrain in the Half-T run produces a weaker windward ridge which creates a weaker pressure gradient between northern and southern Taiwan and a weaker barrier jet in northwestern Taiwan.

b. *Impacts on rainfall by the barrier jet*

The impact of the barrier jet on the mei-yu front and rainfall is most prominent upon the onshore approach of the mei-yu front in this case. Tracking the mei-yu front on land and close to complex terrain is difficult and is often omitted in favor of tracking the front only over the ocean (Wang et al. 2012). A new method was needed to better track the front over land. Therefore, a modified form of the Parfitt et al. (2017) frontal diagnostic will be used at 900 hPa:

$$F = \frac{F^*}{f|\nabla T|_0}, \tag{5}$$

with

$$F^* = \zeta_p|\nabla(\theta_e)|, \tag{6}$$

$$\zeta_p = \left(\frac{\partial v}{\partial x} - \frac{\partial u}{\partial y}\right)_p, \tag{7}$$

$$|\nabla T|_0 = \frac{0.45\ \text{K}}{100\ \text{km}}, \tag{8}$$

where the thermal variable in F^* was changed from temperature to equivalent potential temperature as the mei-yu front has a less defined thermal gradient compared to midlatitude fronts. Should the frontal diagnostic go above a value of 1, there is confidence of a mei-yu front being present. There are numerous methods of tracking the mei-yu front (Ninomiya 1984; Cho and Chen 1995), most of which are modified forms of frontogenesis. Unfortunately, since these frontogenetic equations often rely on deformation of flow along the front, orographic deformation can be misconstrued as a front as well. Therefore, this modified form of the Parfitt et al. (2017) method works best for this study. The use of the diagnostic is not appropriate for determining the strength of the front and is only used for determining the location of the front.

The mei-yu front is aligned along the northwest coastline, extending west into the Taiwan Strait at approximately 1900 UTC 1 June 2017 in both model runs (Figs. 10a,b). In the next hour, heavy rainfall is spatially correlated with the location of the front. The eastern edge of the mei-yu front is coincident with a mesolow on the northernmost coastlines near the Yang-Ming Mountains. Wind barbs at 900 hPa reveal that at this time, the barrier jet is approximately 5–10 kt stronger in the Control run pointing toward the northeast. Downstream of the barrier jet, lighter rainfall is present over the next few hours.

Two hours later at 2100 UTC 1 June 2017, the mei-yu front on land remains at the same location along the northwestern coastline in the Control run whereas the Half-T front has begun to progress southward (Figs. 10c,d). Both model runs have the fronts off the western coast progressing south, however. Despite the Half-T front progressing south on land, there is a small portion that is still present to the north of Yang-Ming Mountains, consistent with the findings of Tu et al. (2022). Heavy rainfall remains linked with the locations of the fronts as well as lighter rainfall downstream of the barrier jet. The barrier jet, approximately located near (24.75°N, 121°E), in the Control run has not changed in strength or size relative to 2 h prior, but the barrier jet in the Half-T run has diminished in both respects in proximity to the mei-yu front.

At 2300 UTC 1 June 2017, the Control mei-yu front is still anchored to the northwestern coastline on land whereas the Half-T front has progressed even farther south (Figs. 10e,f). Similar to 2 h prior, the fronts over the ocean continue to progress south. Unlike prior hours, the location of heavy rainfall in the Control run is only collocated with the off-coast front. On land, the rainfall maximum is displaced south from the frontal diagnostic that remains on the northern coastline, but forms downstream of the off-coast front and its collocated rainfall maximum. In the Half-T run, the heavy rainfall is linked to both the on-land and off-coast fronts, with the mesolow situated on the eastern edge of the front intensifying postfrontal northeasterlies enough to reorient the front on land from west-northwest to east-southeast. The Control barrier jet has not diminished in strength, but the Half-T jet has regained some strength similar to 4 h prior. The lighter precipitation downstream of the barrier jets has remained the same for the Control run, but the Half-T run has the downstream precipitation shifted south with the progression of the mei-yu front. Precipitation along the northern most coastlines has subsided for the Half-T run.

For most of the mei-yu front's period in northern Taiwan, the heaviest rainfall remains linked with the location of the mei-yu front. Despite modifying the terrain height, differences in rainfall intensity over this period are minor. Therefore, the decrease in rainfall duration in the Half-T run can be attributed to the mei-yu front's faster progression on land, consistent with Tu et al. (2022). Their study also suggested the marine boundary layer jet contributing to intense rainfall in northern Taiwan when in contact with the terrain during this case. However, of the types of jet present during this case (i.e., synoptic, marine boundary layer, and barrier jets), the barrier jet is most directly tied to orography and is shown to halt the front at 900 hPa in northern Taiwan in the Control run. Overall, the reduction in terrain height found in the Half-T run resulted in a weaker barrier jet manifesting from weaker upstream orographic deformation in comparison to the Control run. This modification to the barrier jet increased the southern propagation speed of the mei-yu front and with it, a decrease in duration of heavy rainfall collocated with front. This finding supports and builds upon prior work on this event by Wang et al. (2021) whereby there is a strong negative correlation with rainfall accumulation in northern Taiwan with mei-yu front speed; although their study did not explicitly separate rainfall duration from intensity. As the front progresses south into central Taiwan, the role of the taller CMR will be explored as the front directly encounters this steep terrain.

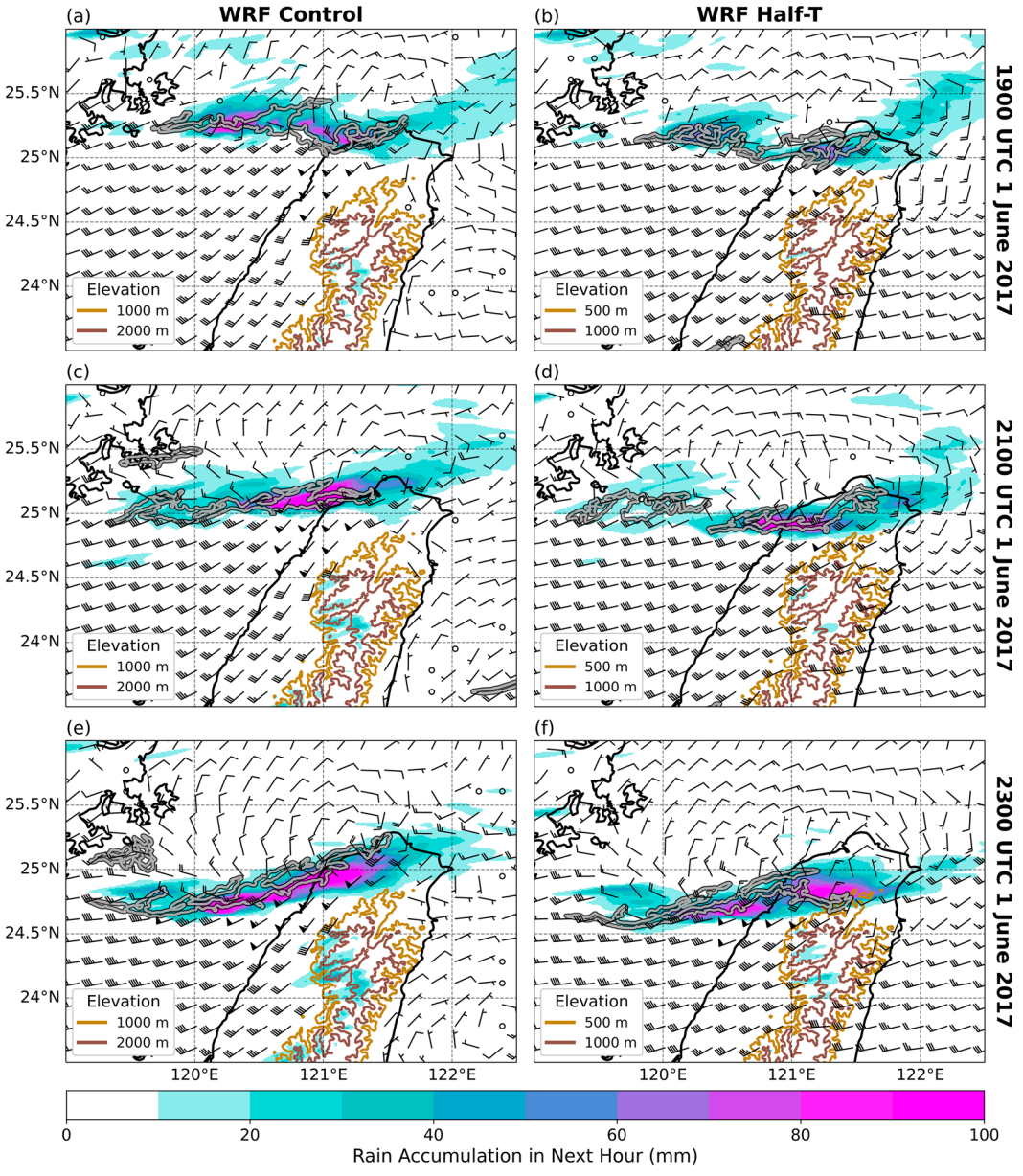

FIG. 10. Wind barbs at 900 hPa, modified Parfitt et al. (2017) frontal diagnostic at 900-hPa values greater than 1 contoured, and rain accumulation over the next hour (in mm) at (a),(b) 1900 UTC 1 Jun; (c),(d) 2100 UTC 1 Jun; and (e),(f) 2300 UTC 1 Jun 2017 for (a),(c),(e) WRF Control and (b),(d),(f) WRF Half-T.

5. Central Taiwan

a. Mei-yu frontal positioning

Although the highest rainfall totals of the June 2017 mei-yu front event occur in central Taiwan, there are no studies that have explored the front as it progresses south past Taipei Basin. Furthermore, mei-yu front progression in central Taiwan is seldom studied, with previous efforts focusing on identifying the front along and off the western coast (Wang et al. 2012). One of the main reasons for this lack of research is in the difficulty of tracking the front on land and near topography, which the modified Parfitt et al. (2017) frontal diagnostic addresses.

The conventional dichotomy of prefrontal southwesterlies and postfrontal northeasterlies found in a mei-yu front breaks down when the front is oriented perpendicular to the CMR. The 900-hPa winds averaged over a 6-h period reveal that while the front is in central Taiwan, typical postfrontal northeasterlies are missing from central to northern Taiwan for both model runs (Fig. 11). In both model runs a leeside cyclone forms to the northeast of Taiwan interrupting possible postfrontal northeasterly winds from reaching the mei-yu front situated on the

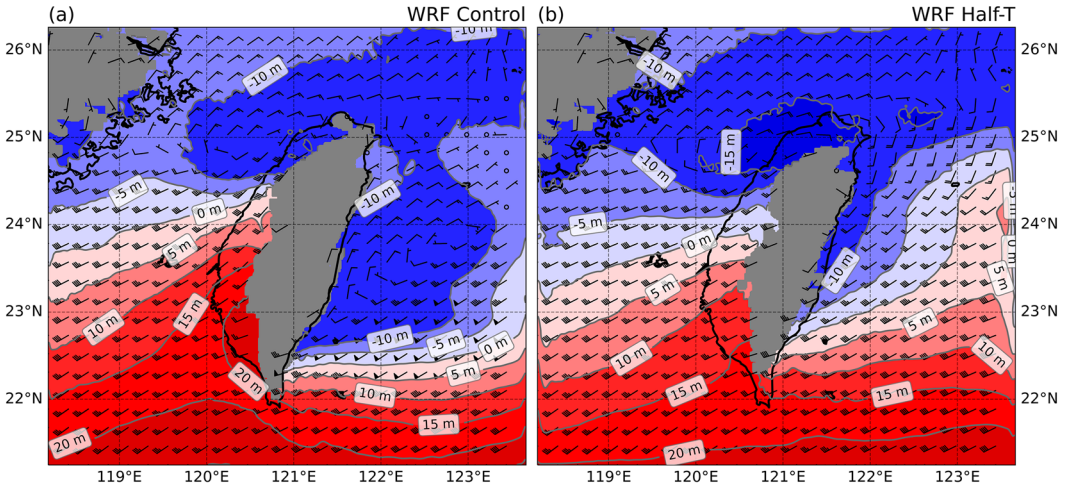

FIG. 11. Average 900-hPa geopotential height anomaly and average wind barbs between 2100 UTC 2 Jun and 0300 UTC 3 Jun 2017 for (a) WRF Control and (b) WRF Half-T.

western slopes of the CMR. This cyclone can be observed in the National Centers for Environmental Prediction Final Operational Global Analysis (Tu et al. 2022). Southwest winds curving around the southern end of the CMR, as well as leeside troughing of southwest winds, may be the cause of this cyclone. Even if the cyclone was not present, postfrontal northeasterlies would likely be orographically blocked by the SMR on approach to central Taiwan. This potential blocking of postfrontal winds would be linked to their weaker magnitude compared to prefrontal southwesterlies which were found to be blocked in northern Taiwan (Figs. 8b and 9b). As such, the mei-yu front will not have a similar prefrontal and postfrontal wind flow as it does in northern Taiwan.

Figures 12 and 13 step through 3 h for both model runs zooming in on west central Taiwan showing wind direction, the modified Parfitt et al. (2017) frontal diagnostic, and wind barbs at 950 hPa. Differences in timing between model runs captures similar starting positions of the fronts identified off the west coast. At the start of analysis for each model run, the mei-yu front, observed at 950 hPa more than 900 hPa (not shown), extends off the western coast of central Taiwan between 23.75° and 24°N (Figs. 12a and 13a). While relatively similar in positioning over the Taiwan Strait, frontal locations are dissimilar on land between model runs. Prefrontal winds are similar between model runs with southwesterly winds between 30 and 35 kt. The postfrontal sectors are drastically different, however. Far to the north of the fronts, there are north-northeasterly winds. Closer to the mei-yu front, they turn counterclockwise, becoming westerlies, which is hypothesized to be the result of frontal deformation. The degree of turning is sharper for the Control run in comparison to the Half-T run, however.

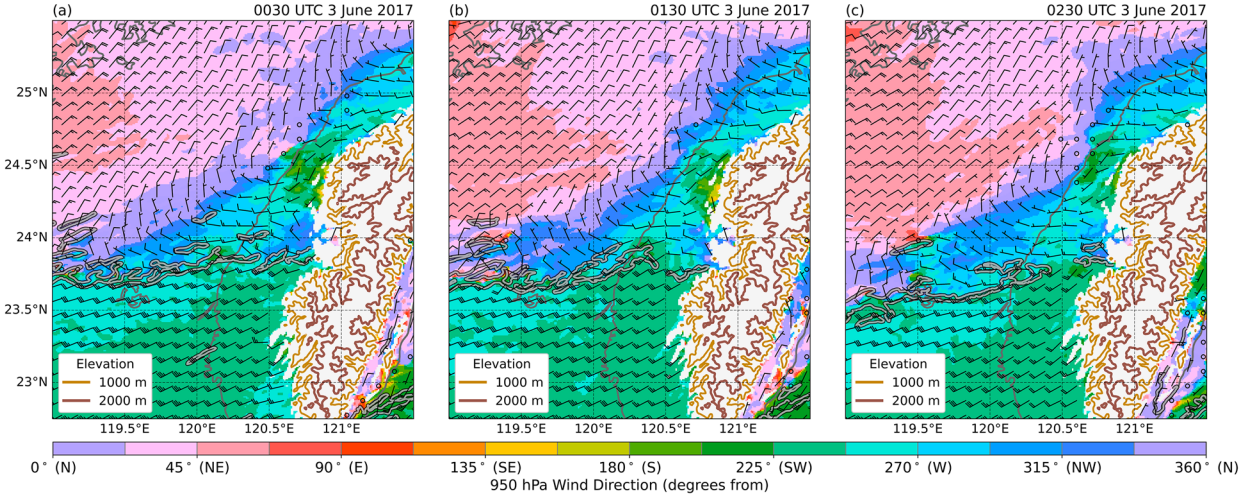

FIG. 12. The 950-hPa wind direction (shading), modified Parfitt et al. (2017) frontal diagnostic at 900-hPa values greater than 1 (contoured), and wind barbs for WRF Control at (a) 0030 UTC 3 Jun, (b) 0130 UTC 3 Jun, and (c) 0230 UTC 3 Jun 2017.

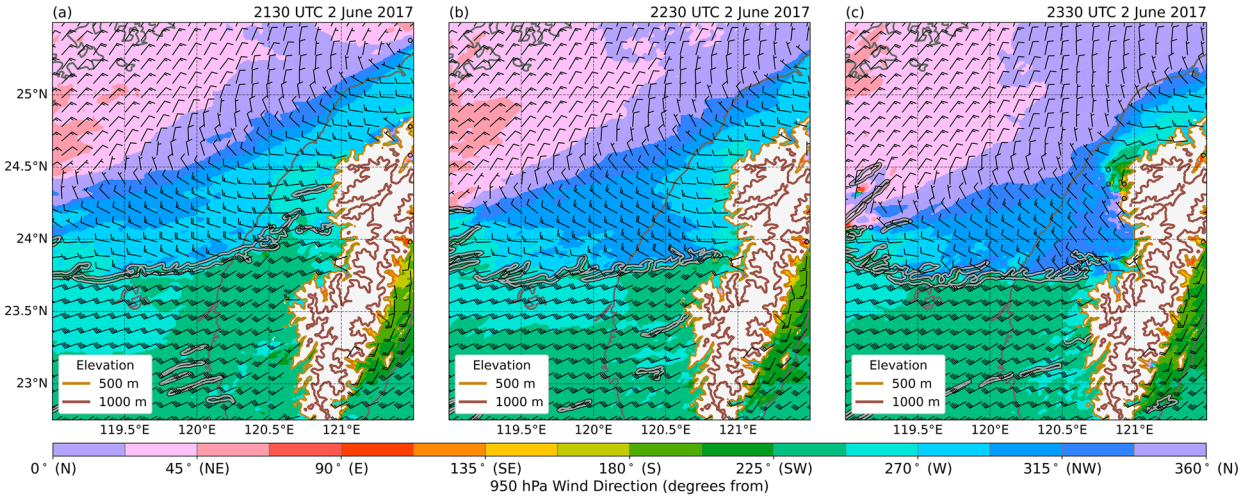

FIG. 13. As in Fig. 12, but for WRF Half-T at (a) 2130 UTC 2 Jun, (b) 2230 UTC 2 Jun, and (c) 2330 UTC 2 Jun 2017.

Thereafter in the Half-T run, postfrontal westerlies run parallel to the mei-yu front, identified by the frontal diagnostic between 24° and 24.5°N, but it is increasingly difficult to pinpoint exactly where the front is located on land. The Control run has a more complex postfrontal sector on land where the postfrontal westerlies encounter the steeper SMR and appear to orographically deform, splitting into south-southwesterly winds to the north and northwesterly winds to the south. These northwest winds collide with the prefrontal southwesterly winds to create a front on land that is not only more easily identifiable than the Half-T run, but is located farther south than the Half-T run closer to 23.75°N.

An hour later, postfrontal northwesterlies begin to emerge in the Half-T run (Fig. 13b), with a more recognizable front on land that is located farther south between 23.75° and 24°N. This front is mostly linear in orientation which contrasts the Control front (Fig. 12b) which has become spatially distorted on land. The front in the Control run is pushed south on land only where we find the postfrontal northwesterlies, which is where postfrontal orographic deformation is suspected based on wind direction shift close to the topography. Therefore, despite the emergence of postfrontal northwesterlies in the Half-T run, the Control front on land and near the terrain is still farther south by comparison.

One more hour later and the Control front near the terrain has not moved much on land despite the front over the ocean progressing south (Fig. 12c). The postfrontal sector of the Half-T run has become almost entirely northwesterly, maintaining a linearly oriented front on land which has progressed farther south than the Control front in the past hour (Fig. 13c). Although the postfrontal sector is likely linked to frontal progression speed, there is likely another contribution from the prefrontal sector with some evidence of stronger orographic deformation in the Control run leading to more southerly winds near the terrain compared to the more westerly winds in the Half-T run. This observation supports a slower southern progression of the Control front on land in comparison to the Half-T front. Although the strength of the postfrontal northwesterlies that form from suspected orographic deformation in the Control run are comparable to that of the Half-T run's postfrontal northwesterlies, the area that the postfrontal northwesterlies cover is different with the Control run only exhibiting northwesterlies close to the topography and the Half-T run having northwesterlies extending far beyond the coastline. The existence of the postfrontal northwesterlies is likely important for maintaining the front and their strength and spatial extent affects frontal progression south. These wind direction trends are prevalent at 925 and 875 hPa as well (not shown).

b. *Impact of frontal positioning on rainfall*

Extreme rainfall in central Taiwan is predominantly focused on higher terrain (Fig. 4) and as such will be the focus of this section in the context of frontal placement which varies between the Control and Half-T runs in this region. Figure 14 shows rainfall accumulation over the next hour for the times discussed in section 5a. At the start of analysis, collocation of extreme rainfall with the mei-yu front, is captured by the Control run (Fig. 14a). This result is similar to the findings in northern Taiwan but extended east of the frontal diagnostic into the topography with rainfall exceeding 60 mm h^{-1}. The Half-T run does not have the heaviest rainfall in the high terrain, but rather upstream of the topography and south of the mei-yu front (Fig. 14d). The rainfall may not be collocated with the front possibly owing to how difficult it is to track the front over land or due to rapid southern propagation of the front.

An hour later and the Half-T run now has heavy rainfall collocated with the mei-yu front, though the rainfall is still shifted upstream of the topography (Fig. 14e). The Control run has extreme rainfall in the CMR to the east of the mei-yu front at 23.8°N, but the Control front is not linear and is not contained at a single latitude (Fig. 14b). It appears the location of the heavier rainfall is determined by the location of the front in direct contact with the topography. This assertion is only consistent for the most extreme rainfall associated with the front.

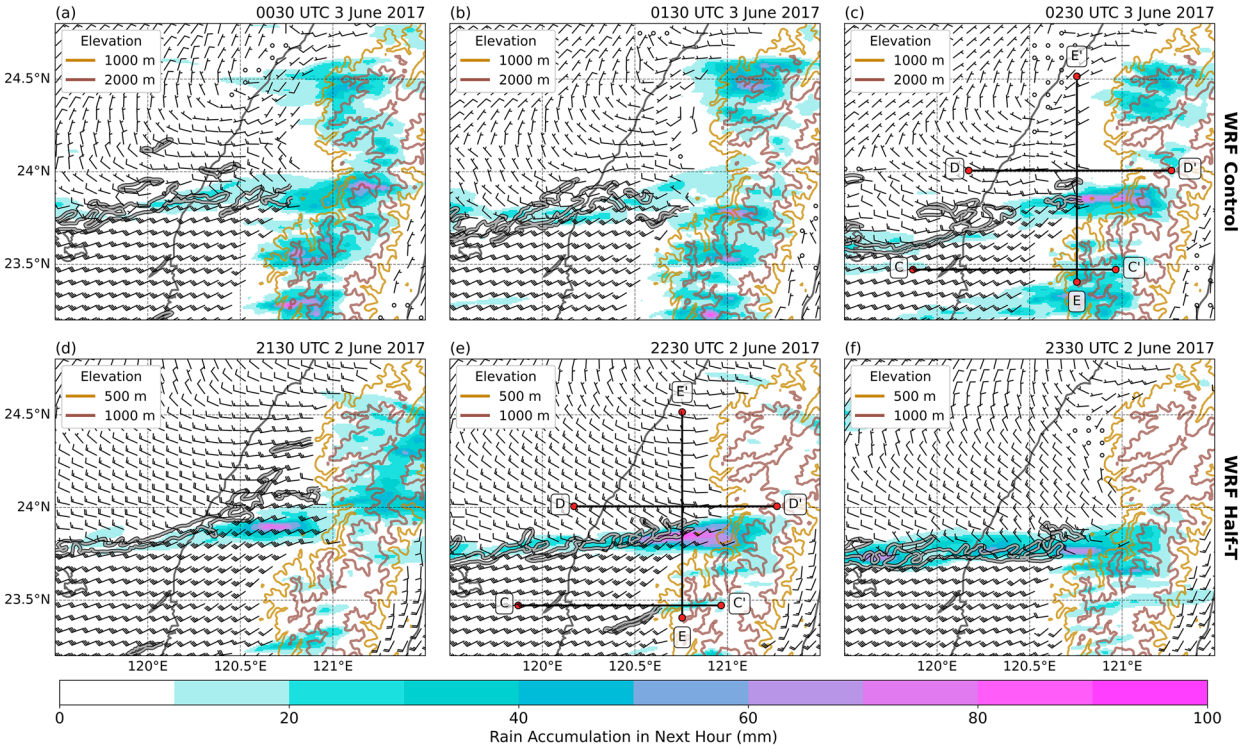

FIG. 14. As in Fig. 10, but at 950 hPa and for (a)–(c) WRF Control at (a) 0030 UTC 3 Jun, (b) 0130 UTC 3 Jun, and (c) 0230 UTC 3 Jun 2017 and (d)–(f) WRF Half-T at (d) 2130 UTC 2 Jun, (e) 2230 UTC 2 Jun, and (f) 2330 UTC 2 Jun 2017. Cross sections are taken along lines CC′, DD′, and EE′.

In the last hour, similar characteristics remain. In the Control run, despite the front appearing to be located along 23.6°N off the western coast, the section of the front closer to the terrain is located just north of 23.8°N (Fig. 14c). In turn, not only is extreme rainfall in the next hour aligned with 23.8°N, but little to no rainfall is observed along 23.6°N, further supporting that the placement of the front off the coast is not directly controlling rainfall location and intensity near the terrain. In the Half-T run, the same observation can be made, but because the front is near zonally oriented, rainfall aligns along a single latitude (Fig. 14f).

At each hour, a common thread remains with extreme rainfall being found to the east of the mei-yu front's location in direct contact with the CMR. As such, the implications this finding has on rainfall are similar to findings in northern Taiwan in that rainfall duration is tied to the propagation speed of the mei-yu front. In the Half-T run, the strong postfrontal northwesterlies with a more westerly prefrontal sector acts to increase frontal propagation speed, thereby decreasing rainfall duration in a given location. The Control run experiences the opposite with the weak postfrontal northwesterlies formed through suspected orographic deformation colliding with a more southerly prefrontal sector, slowing frontal propagation and increasing rainfall duration at a given location.

c. *Orographic deformation*

To validate hypotheses of orographic deformation in the prefrontal and postfrontal sector that were shown in the previous section to have possible implications for rainfall location near the steep terrain, cross sections are presented from off the coast toward the CMR on both sides of the mei-yu front (Figs. 15 and 16). The cross-front difference in orographic blocking is most apparent due to the different maximum terrain heights of the SMR in the postfrontal sector and the CMR in the prefrontal sector. In viewing the zonal wind of the prefrontal sector, both model runs exhibit similar wind speeds under 0.5 km MSL, but above that level, the Half-T run (Fig. 15d) is approximately 10 m s^{-1} faster than the Control run (Fig. 15c). A consequence of this difference, along with the differences in terrain height, is that the blocking height, as viewed through the zonal, altitude-relative Froude number, is significantly higher in the prefrontal sector of the Control run (Fig. 15a) relative to the Half-T run (Fig. 15b). For much of the Control prefrontal sector, the blocking height is near 2.5 km whereas much of the Half-T sector is only blocked up to 0.5 km with regions close to the terrain being unblocked.

Zonal wind speeds in the prefrontal and postfrontal sectors are similar above 1 km MSL, but beneath that level, both model runs have postfrontal easterly flow in the west turning into westerly flow in the east indicative of the counterclockwise turning (Figs. 16c,d). The wind speeds below 1 km are not all that dissimilar between the Half-T and Control run; therefore, the differences in Froude number are likely attributed to the differences in terrain height with the Control run having a higher blocking height relative to the Half-T run. Therefore, a reason why the

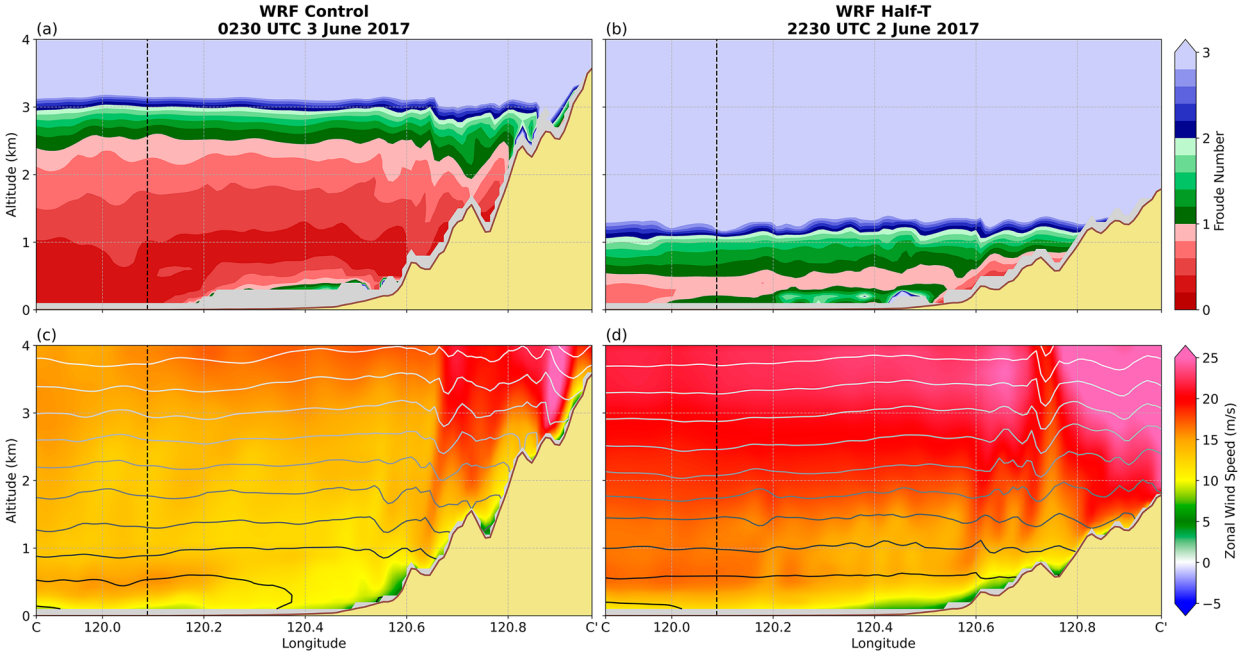

FIG. 15. Zonal cross sections along CC′ in Fig. 14. (a),(b) Zonal cross sections of height-relative Froude number and (c),(d) Zonal cross sections of zonal wind speed with dry isentropes. The dashed black line indicates the coastline.

Control front has a slower propagation speed is because of stronger conversion of westerly flow to southerly flow via orographic blocking in the prefrontal sector.

When viewing the mei-yu front along a meridian, differences in the prefrontal and postfrontal sectors are more striking (Fig. 17). The gradient in zonal and meridional wind speeds found near 23.85°N indicates the approximate location of the mei-yu front. Differences in these gradients among model runs also manifests in how sharp of a cross-front isentropic gradient exists given the Control gradient is much sharper than the Half-T gradient at low levels. In the prefrontal sectors, zonal winds are approximately 10 m s^{-1} weaker in

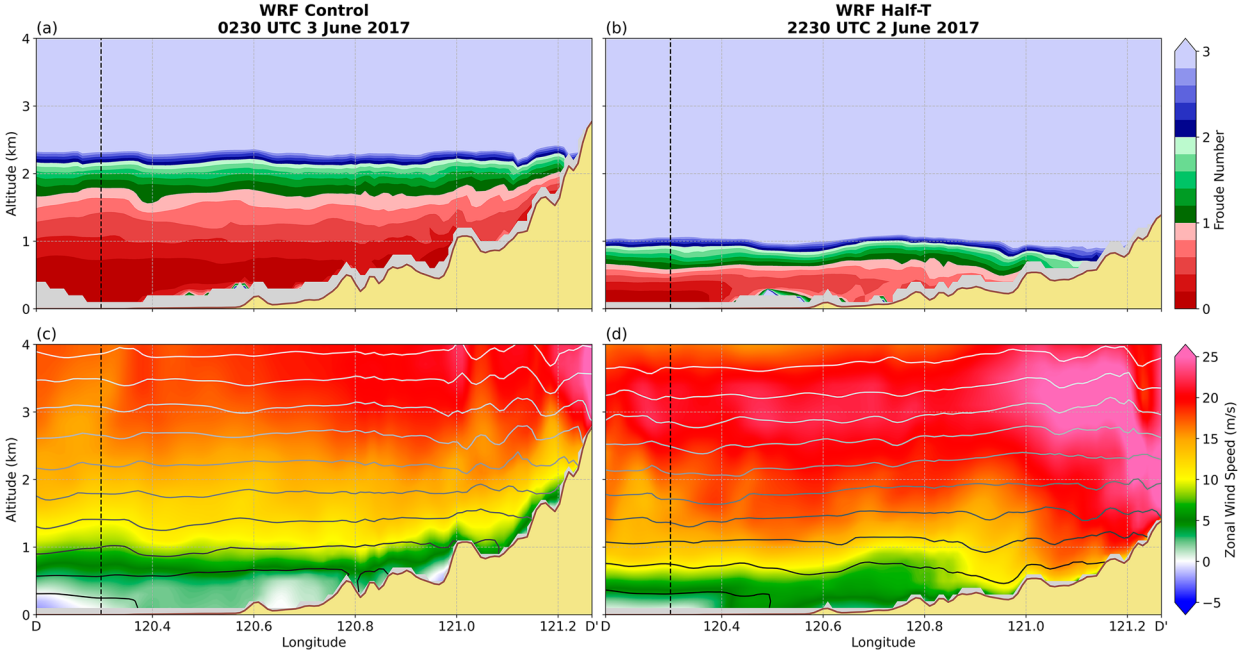

FIG. 16. As in Fig. 15, but for cross section DD′ in Fig. 14.

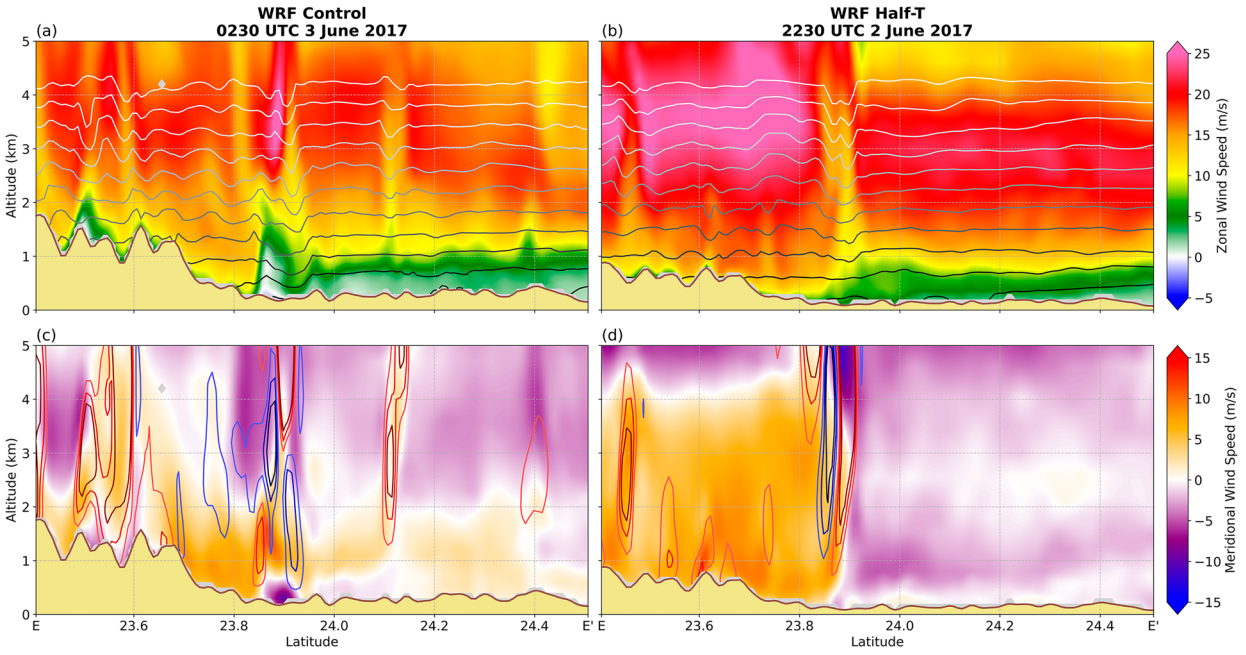

FIG. 17. Meridional cross sections along EE′ in Fig. 14. (a),(b) Meridional cross sections of zonal wind speed with dry isentropes and (c),(d) meridional cross sections of meridional wind speed with vertical velocity.

the Control run compared to the Half-T run throughout all levels, consistent with stronger orographic blocking (Figs. 17a,b). The postfrontal sectors only differ by 5 m s^{-1} in comparison, but the Control run has near stagnant flow near the surface that is absent the Half-T run. The steeper terrain in the Control run leads to more complex meridional winds along this cross section relative to the Half-T run (Figs. 17c,d). The wind speeds of the prefrontal southerlies in direct contact with the front are relatively similar, however. Winds in the Control run's postfrontal sector clearly illuminate orographic deformation near 24.15°N (Fig. 17c). This relationship can be assumed because of northerlies to the south, southerlies in the north, and positive vertical velocity found at the gradient between the two. In contrast, the entirety of the Half-T postfrontal sector is weakly northerly (Fig. 17d). Interestingly, there is a strong postfrontal northerly flow relative to the other northerlies in the postfrontal sectors just north of the Control front that seems to not be connected to northerlies that form from orographic deformation.

A proposed reason for higher duration of rainfall in the Control run is therefore due to a slowdown of the mei-yu front's southern propagation (Fig. 18). Similar to northern Taiwan, heavier rainfall is collocated with the front (Fig. 18a), but heavier rainfall is also correlated downstream of the front's location in proximity to the CMR in central Taiwan (Fig. 18b). Therefore, by slowing the front in central Taiwan, the rainfall duration increases where the front remains quasi-stationary. In the Half-T run, the strength and areal coverage of northwesterly postfrontal flow pushes the front south. Furthermore, the more northerly the postfrontal flow, the greater the southern propagation of the mei-yu front. The Control run has weak northwesterly postfrontal flow that does not extend far from the CMR owing to orographic deformation of the postfrontal flow. The Half-T run has stronger northwesterly flow in the postfrontal sector that spans beyond the coastline, acting to push the front south faster than the Control run. In the prefrontal sectors, the Control run experiences slightly greater orographic blocking which creates orographic deformation in proximity to the CMR. This deformation acts to create more southerly flow in the prefrontal sector that resists southern propagation in the Control run as opposed to the Half-T run, increasing rainfall duration.

An explanation as to why these postfrontal sectors appear different is still not well understood. One explanation for these postfrontal wind differences between runs is found in the northern half of the postfrontal orographic deformation in the Control run. The postfrontal orographic deformation forms southerlies upon colliding with the CMR. These southerlies along with north-northeasterly winds in northern Taiwan create a small cyclone with clockwise rotation in the postfrontal sector (Fig. 12). This pattern creates a bit of a dilemma, however, since the orographic deformation seen in the postfrontal sector of the Control run relies on turning of postfrontal winds into westerlies. This scenario could be considered a "chicken or the egg" situation whereby the westerlies leading to orographic deformation are attributed to a cyclone, but the cyclone is induced by the orographic deformation. Other explanations could be differences in model runs after initialization as well as differences in the leeside cyclone strength. Regardless, explaining how these postfrontal and prefrontal flows converge determines frontal propagation speed and in turn, contributes to the duration of rainfall in central Taiwan. Whereas the front was halted by the barrier jet found in the prefrontal sector in northern Taiwan, the slowing of the Control front in central Taiwan for this case is attributed to

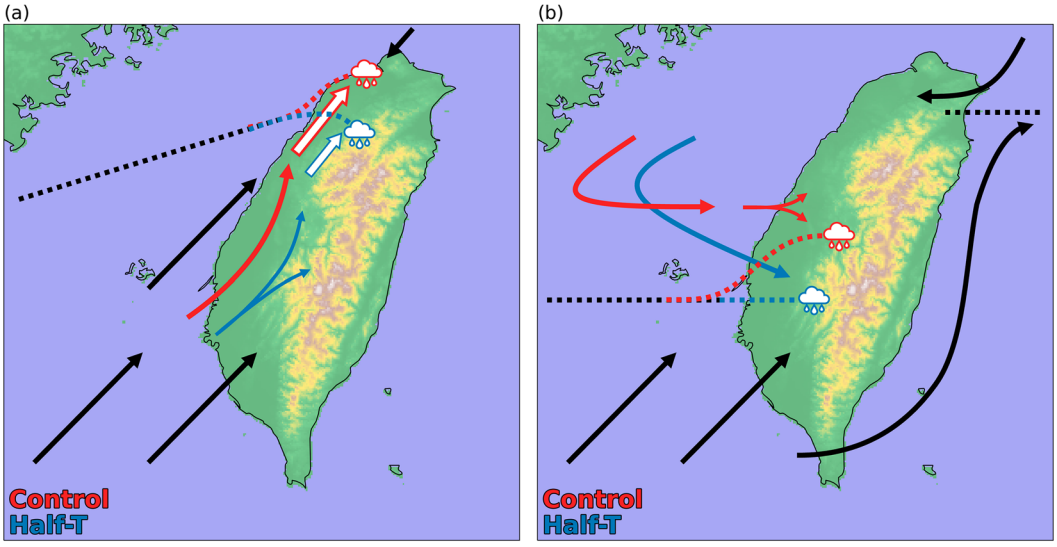

FIG. 18. Schematics representing the effect of halving terrain on low-level flow and mei-yu front progression in (a) northern Taiwan and (b) central Taiwan. Filled arrows represent low-level flow and dashed lines represent the position of the mei-yu front. Unfilled arrows represent the barrier jet in northern Taiwan. Red and blue represent deviations between model runs for Control and Half-T, respectively.

weaker postfrontal meridional flow and stronger prefrontal meridional flow. Determining which relationship is more dominant in this region of steep topography will be a future research topic with additional case studies.

6. Conclusions

Between 1 and 3 June 2017, a strong mei-yu front moved onto the northern coastline of Taiwan and progressed south through the island. This front produced extreme amounts of rainfall creating widespread damage to infrastructure and endangered the populace. Notable regions of impact were the northern coastline receiving upward of 600 mm of rainfall in a 12-h span and central Taiwan where the maximum 48-h rainfall recorded was found in the CMR with approximately 1500 mm of rainfall. This event captured both aspects of extreme rainfall—high duration and high intensity—and acts as an ideal case to study orographic influences on extreme precipitation.

This event was simulated using the WRF Model to create a Control run and an experimental run (Half-T) where the terrain height was halved to determine orographic influences on rainfall intensity, duration, and location during this event. The key findings are as follows:

1) The strength of the orographically induced barrier jet was decreased for reduced terrain height. This weakened barrier jet was not able to resist southern propagation of the mei-yu front in northern Taiwan compared to the stronger barrier jet in the Control run.
2) In central Taiwan, orographic deformation on both sides of the Control front slowed southern propagation of the mei-yu front while the stronger postfrontal winds of the Half-T run pushed the front south.
3) In both northern and central Taiwan, propagation of the mei-yu front was faster in the Half-T run. With a faster propagation speed, collocated frontal rainfall is spread out over a greater area, decreasing rainfall duration.

While there are many differences between each model run's mei-yu front, the low level wind appears to control much of that difference. The decrease in rainfall duration in northern Taiwan with a decrease in rainfall duration is attributed to a decrease in the barrier jet strength. Orographic blocking of monsoonal, southwesterly flow in central and southern Taiwan, diverts flow downstream to northwestern Taiwan where it converges with the mean flow to induce a jet at low levels (Fig. 18a). With a reduction in terrain height, the orographic blocking in central and southern Taiwan is weakened, resulting in weaker diversion of flow to northern Taiwan, manifesting in a barrier jet that is 5–10 kt weaker than the Control run. With a weaker barrier jet, the prefrontal flow is less resistant to the mei-yu front's southern advancement, thus the front's propagation speed is faster than in the Control run. The most intense rainfall is collocated with the location of the front. Therefore, by speeding up the propagation speed of the front, rainfall duration drops in the Half-T run while in northern Taiwan.

No previous studies have explored the mei-yu front and influence on rainfall in Central Taiwan for this extreme rainfall case. Furthermore, there are no studies that explore the front near the CMR or more generally, the dynamics of any front whose orientation is perpendicular to a mountain range. Therefore, the results of this case study focusing on central Taiwan are a first step in addressing this gap in the literature. The decrease in terrain height results in a decrease in rainfall duration and intensity in central Taiwan. Much like northern Taiwan, extreme rainfall is tethered to the location of the mei-yu front and rainfall duration is inversely correlated to the mei-yu front's propagation

speed. Propagation speed is linked to both prefrontal and postfrontal differences in flow. Differences in prefrontal flow are attributed to differences in orographic deformation strength. Whereas most of the Half-T postfrontal sector converges with prefrontal flow, the only portion of the Control run's postfrontal sector that converges with the prefrontal sector is flow that orographically deforms (Fig. 18b). All of these assertions are in proximity to the CMR and rainfall in the CMR is linked to the location of the front near the terrain regardless of where the front is over the ocean.

Although there are apparent differences in rainfall intensity in central Taiwan (Fig. 6), parsing out what contributes to those differences is difficult. While frontal placement is linked to duration, as heavy rainfall was found to be collocated with the front, light rainfall also was nearly constantly observed in the SMR and CMR in the Control run, contributing to the overall rainfall accumulation. This rainfall was not as predominant in the Half-T run, likely owing to the decrease in orographic lift, which overall can influence rainfall intensity. Despite the 5–10-kt difference in the prefrontal flow attributed to the barrier jet strengths in northern Taiwan, that presumably would lead to stronger convergence in the Control run and in turn, stronger lift and precipitation, but intensity differences in northern Taiwan between runs were not as evident as central Taiwan. A potential reasoning for this could be rooted in how intensity and duration is defined, especially considering the Eulerian approach taken in this study. Determining the orographic impact on rainfall intensity will be expanded on in future studies. These differences between central Taiwan and northern Taiwan may also be attributed to the escalation of small perturbations at different time scales beyond the initialization time.

Furthermore, while the mesoscale aspects of this event were faithfully reproduced, the microscale was not, with exaggerated amounts of ice hydrometeors produced in WRF when compared to radar-inferred hydrometeors. A possible by-product of this misrepresentation of the microphysics is a lack of postfrontal stratiform precipitation in northern Taiwan that is observed in the operational radars. This lack of stratiform precipitation has implications for rainfall duration and intensity. As such, next steps will compare microphysics schemes to address this problem and begin assessing how altering the terrain height modifies the microphysical structure of precipitation in and outside of the mei-yu front in proximity to terrain. Previous studies have already shown that single moment microphysical schemes can outperform double moment schemes in producing heavy rainfall in moist, tropical environments (Zhang et al. 2022).

Expanding outside of this event, the findings of this study will be compared with data collected during the 2022 Prediction of Rainfall Extremes Campaign in the Pacific (PRECIP 2022), including mei-yu front events that exhibited high rainfall accumulations but with varying intensities and durations. The high temporal and vertical resolution of the NSF/NCAR S-band dual-polarization radar, S-Pol, deployed during PRECIP 2022 will further allow for analysis of microphysical processes in the intensity–duration framework that produced extreme rainfall in Taiwan's complex terrain.

Acknowledgments. This study was supported by the NOAA Cooperative Institute for Meteorological Satellite Studies through their graduate student education program and National Science Foundation Awards AGS-2013743, AGS-1854399, and AGS-1854559. We would like to acknowledge high-performance computing support from Cheyenne (doi: 10.5065/D6RX99HX) provided by NCAR's Computational and Information Systems Laboratory, sponsored by the National Science Foundation. The authors thank Alison Nugent, Tianqi Zuo, Zoe Douglas, Rung Panasawatwong, and Hungjui Yu for their helpful feedback as well as the Central Weather Administration for providing QPESUMS and radar data. The authors would also like to thank the two anonymous reviewers for their insightful feedback and comments.

Data availability statement. QPESUMS and radar data are available by request from the CWA. A subset of the 1-km WRF simulations along with the WRF namelists will be made available through Dryad upon publication. The full 1-km WRF simulations and WRF namelists are available upon request.

REFERENCES

Arakane, S., H.-H. Hsu, C.-Y. Tu, H.-C. Liang, Z.-Y. Yan, and S.-J. Lin, 2019: Remote effect of a tropical cyclone in the Bay of Bengal on a heavy-rainfall event in subtropical East Asia. *Nature*, **2**, 25, https://doi.org/10.1038/s41612-019-0082-8.

Bell, M., 2022: nsf-lrose/lrose-topaz: lrose-topaz-20220222. Zenodo, accessed 24 June 2022, https://doi.org/10.5281/ZENODO.6909478.

Chang, C.-P., and G. T.-J. Chen, 1995: Tropical circulations associated with southwest monsoon onset and westerly surges over the South China Sea. *Mon. Wea. Rev.*, **123**, 3254–3267, https://doi.org/10.1175/1520-0493(1995)123<3254:TCAWSM>2.0.CO;2.

Chang, P.-L., and Coauthors, 2021: An operational multi-radar multi-sensor QPE system in Taiwan. *Bull. Amer. Meteor. Soc.*, **102**, E555–E577, https://doi.org/10.1175/BAMS-D-20-0043.1.

Chen, G. T.-J., 1983: Observational aspects of the Mei-Yu phenomenon in subtropical China. *J. Meteor. Soc. Japan*, **61**, 306–312, https://doi.org/10.2151/jmsj1965.61.2_306.

——, 1992: Mesoscale features observed in the Taiwan Mei-Yu season. *J. Meteor. Soc. Japan*, **70**, 497–516, https://doi.org/10.2151/jmsj1965.70.1B_497.

——, 1994: Large-scale circulations associated with the East Asian summer monsoon and the Mei-Yu over South China and Taiwan. *J. Meteor. Soc. Japan*, **72**, 959–983, https://doi.org/10.2151/jmsj1965.72.6_959.

Chen, S.-H., and Y.-L. Lin, 2005: Effects of moist Froude number and CAPE on a conditionally unstable flow over a mesoscale mountain ridge. *J. Atmos. Sci.*, **62**, 331–350, https://doi.org/10.1175/JAS-3380.1.

——, ——, and Z. Zhao, 2008: Effects of unsaturated moist Froude number and orographic aspect ratio on a conditionally unstable flow over a mesoscale mountain. *J. Meteor. Soc. Japan*, **86**, 353–367, https://doi.org/10.2151/jmsj.86.353.

Chen, S.-J., Y.-H. Kuo, W. Wang, Z.-Y. Tao, and B. Cui, 1998: A modeling case study of heavy rainstorms along the mei-yu front. *Mon. Wea. Rev.*, **126**, 2330–2351, https://doi.org/10.1175/1520-0493(1998)126<2330:AMCSOH>2.0.CO;2.

Chen, Y.-L., 1993: Some synoptic-scale aspects of the surface fronts over southern China during TAMEX. *Mon. Wea. Rev.*,

121, 50–64, https://doi.org/10.1175/1520-0493(1993)121<0050:SSSAOT>2.0.CO;2.

——, C.-C. Tu, F. Hsiao, C.-S. Chen, P.-L. Lin, and P.-H. Lin, 2022: An overview of Low-Level Jets (LLJs) and their roles in heavy rainfall over the Taiwan area during the early summer rainy season. *Meteorology*, **1**, 64–112, https://doi.org/10.3390/meteorology1010006.

Cho, H.-R., and G. T. J. Chen, 1995: Mei-yu frontogenesis. *J. Atmos. Sci.*, **52**, 2109–2120, https://doi.org/10.1175/1520-0469(1995)052<2109:MYF>2.0.CO;2.

Chung, K.-S., H.-J. Liu, C.-Y. Liu, and M.-Y. Lin, 2020: Satellite observation for evaluating cloud properties of the microphysical schemes in weather research and forecasting simulation: A case study of the Mei-Yu front precipitation system. *Remote Sens.*, **12**, 3060, https://doi.org/10.3390/rs12183060.

Davis, C. A., and W.-C. Lee, 2012: Mesoscale analysis of heavy rainfall episodes from SoWMEX/TiMREX. *J. Atmos. Sci.*, **69**, 521–537, https://doi.org/10.1175/JAS-D-11-0120.1.

Dixon, M., and W.-C. Lee, 2016: CfRadial data file format: CF-compliant netCDF format for moments data for RADAR and LIDAR in radial coordinates. NCAR/UNIDATA, NCAR Tech. Rep., 74 pp., https://opensky.ucar.edu/islandora/object/manuscripts%3A997/datastream/PDF/view.

Doswell, C. A., III, H. E. Brooks, and R. A. Maddox, 1996: Flash flood forecasting: An ingredients-based methodology. *Wea. Forecasting*, **11**, 560–581, https://doi.org/10.1175/1520-0434(1996)011<0560:FFFAIB>2.0.CO;2.

Helmus, J. J., and S. M. Collis, 2016: The Python ARM radar toolkit (Py-ART), a library for working with weather radar data in the Python programming language. *J. Open Res. Software*, **4**, e25, https://doi.org/10.5334/jors.119.

Henny, L., C. D. Thorncroft, H.-H. Hsu, and L. F. Bosart, 2021: Extreme rainfall in Taiwan: Seasonal statistics and trends. *J. Climate*, **34**, 4711–4731, https://doi.org/10.1175/JCLI-D-20-0999.1.

Hong, S.-Y., Y. Noh, and J. Dudhia, 2006: A new vertical diffusion package with an explicit treatment of entrainment processes. *Mon. Wea. Rev.*, **134**, 2318–2341, https://doi.org/10.1175/MWR3199.1.

Iacono, M. J., J. S. Delamere, E. J. Mlawer, M. W. Shephard, S. A. Clough, and W. D. Collins, 2008: Radiative forcing by long-lived greenhouse gases: Calculations with the AER radiative transfer models. *J. Geophys. Res.*, **113**, D13103, https://doi.org/10.1029/2008JD009944.

Janić, Z. I., 2001: Nonsingular implementation of the Mellor-Yamada level 2.5 scheme in the NCEP Meso model. NCEP Office Note 437, 61 pp., https://repository.library.noaa.gov/view/noaa/11409.

Jhun, J.-G., and E.-J. Lee, 2004: A new East Asian winter monsoon index and associated characteristics of the winter monsoon. *J. Climate*, **17**, 711–726, https://doi.org/10.1175/1520-0442(2004)017<0711:ANEAWM>2.0.CO;2.

Jou, B. J.-D., W.-C. Lee, and R. H. Johnson, 2011: An overview of SOWMEX/TIMREX. *The Global Monsoon System: Research and Forecast*, C.-P. Chang et al., Eds., World Scientific, 303–318, https://doi.org/10.1142/9789814343411_0018.

Ke, C.-Y., K.-S. Chung, T.-C. C. Wang, and Y.-C. Liou, 2019: Analysis of heavy rainfall and barrier-jet evolution during Mei-Yu season using multiple Doppler radar retrievals: A case study on 11 June 2012. *Tellus*, **71A**, 1571369, https://doi.org/10.1080/16000870.2019.1571369.

Kirshbaum, D. J., B. Adler, N. Kalthoff, C. Barthlott, and S. Serafin, 2018: Moist orographic convection: Physical mechanisms and links to surface-exchange processes. *Atmosphere*, **9**, 80, https://doi.org/10.3390/atmos9030080.

Kuo, Y.-H., and G. T.-J. Chen, 1990: The Taiwan Area Mesoscale Experiment (TAMEX): An overview. *Bull. Amer. Meteor. Soc.*, **71**, 488–503, https://doi.org/10.1175/1520-0477(1990)071<0488:TTAMEA>2.0.CO;2.

Ladwig, W., 2017: WRF-Python (version 1.3. 2.). UCAR/NCAR, accessed 18 August 2022, https://doi.org/10.5065/D6W094P1.

Lau, K.-M., G. J. Yang, and S. H. Shen, 1988: Seasonal and intraseasonal climatology of summer monsoon rainfall over East Asia. *Mon. Wea. Rev.*, **116**, 18–37, https://doi.org/10.1175/1520-0493(1988)116<0018:SAICOS>2.0.CO;2.

Li, J., and Y.-L. Chen, 1998: Barrier jets during TAMEX. *Mon. Wea. Rev.*, **126**, 959–971, https://doi.org/10.1175/1520-0493(1998)126<0959:BJDT>2.0.CO;2.

Lin, Y.-L., 1993: Orographic effects on airflow and mesoscale weather systems over Taiwan. *Terr. Atmos. Oceanic Sci.*, **4**, 381–420, https://doi.org/10.3319/TAO.1993.4.4.381(A).

——, S. Chiao, T.-A. Wang, M. Kaplan, and R. Weglarz, 2001: Some common ingredients for heavy orographic rainfall. *Wea. Forecasting*, **16**, 633–660, https://doi.org/10.1175/1520-0434(2001)016<0633:SCIFHO>2.0.CO;2.

Marín, J. C., B. S. Barrett, and D. Pozo, 2021: The tornadoes of 30–31 May 2019 in south-central Chile: Sensitivity to topography and SST. *Atmos. Res.*, **249**, 105301, https://doi.org/10.1016/j.atmosres.2020.105301.

May, R., and Coauthors, 2022: MetPy: A meteorological Python library for data analysis and visualization. *Bull. Amer. Meteor. Soc.*, **103**, E2273–E2284, https://doi.org/10.1175/BAMS-D-21-0125.1.

Ninomiya, K., 1984: Characteristics of Baiu front as a predominant subtropical front in the summer Northern Hemisphere. *J. Meteor. Soc. Japan*, **62**, 880–894, https://doi.org/10.2151/jmsj1965.62.6_880.

Parfitt, R., A. Czaja, and H. Seo, 2017: A simple diagnostic for the detection of atmospheric fronts. *Geophys. Res. Lett.*, **44**, 4351–4358, https://doi.org/10.1002/2017GL073662.

Paul, S., C.-C. Wang, L.-S. Tseng, D.-I. Lee, J.-S. Hong, and T.-M. Leou, 2021: Evaluation of rainfall forecasts by three mesoscale models during the Mei-Yu season of 2008 in Taiwan. Part I: Subjective comparison. *Asia-Pac. J. Atmos. Sci.*, **57**, 817–838, https://doi.org/10.1007/s13143-021-00229-2.

Pierrehumbert, R. T., 1984: Linear results on the barrier effects of mesoscale mountains. *J. Atmos. Sci.*, **41**, 1356–1367, https://doi.org/10.1175/1520-0469(1984)041<1356:LROTBE>2.0.CO;2.

——, and B. Wyman, 1985: Upstream effects of mesoscale mountains. *J. Atmos. Sci.*, **42**, 977–1003, https://doi.org/10.1175/1520-0469(1985)042<0977:UEOMM>2.0.CO;2.

Reinecke, P. A., and D. R. Durran, 2008: Estimating topographic blocking using a Froude number when the static stability is nonuniform. *J. Atmos. Sci.*, **65**, 1035–1048, https://doi.org/10.1175/2007JAS2100.1.

Riley Dellaripa, E. M., E. D. Maloney, B. A. Toms, S. M. Saleeby, and S. C. van den Heever, 2020: Topographic effects on the Luzon diurnal cycle during the BSISO. *J. Atmos. Sci.*, **77**, 3–30, https://doi.org/10.1175/JAS-D-19-0046.1.

Skamarock, W. C., and Coauthors, 2019: A description of the Advanced Research WRF Model version 4. NCAR Tech. Note NCAR/TN-556+STR, 165 pp., https://doi.org/10.5065/1dfh-6p97.

Tao, S.-Y., 1987: A review of recent research on the East Asian summer monsoon. *Monsoon Meteorology*, C. P. Chang and T. N. Krishnamurti, Eds., Oxford University Press, 60–92.

Tewari, M., and Coauthors, 2004: Implementation and verification of the unified Noah land surface model in the WRF model. *20th Conf. on Weather Analysis and Forecasting/16th Conf. on Numerical Weather Prediction*, Seattle, WA, Amer. Meteor. Soc., 14.2A, https://ams.confex.com/ams/84Annual/techprogram/paper_69061.htm.

Thompson, G., and T. Eidhammer, 2014: A study of aerosol impacts on clouds and precipitation development in a large winter cyclone. *J. Atmos. Sci.*, **71**, 3636–3658, https://doi.org/10.1175/JAS-D-13-0305.1.

Tu, C.-C., Y.-L. Chen, P.-L. Lin, and P.-H. Lin, 2020: The relationship between the boundary layer moisture transport from the South China Sea and heavy rainfall over Taiwan. *Terr. Atmos. Oceanic Sci.*, **31**, 159–176, https://doi.org/10.3319/TAO.2019.07.01.01.

——, ——, ——, and M.-Q. Huang, 2022: Analysis and simulations of a heavy rainfall event associated with the passage of a shallow front over northern Taiwan on 2 June 2017. *Mon. Wea. Rev.*, **150**, 505–528, https://doi.org/10.1175/MWR-D-21-0113.1.

Tung, Y.-S., C.-Y. Wang, S.-P. Weng, and C.-D. Yang, 2022: Extreme index trends of daily gridded rainfall dataset (1960–2017) in Taiwan. *Terr. Atmos. Oceanic Sci.*, **33**, 8, https://doi.org/10.1007/s44195-022-00009-z.

Viale, M., R. A. Houze Jr., and K. L. Rasmussen, 2013: Upstream orographic enhancement of a narrow cold-frontal rainband approaching the Andes. *Mon. Wea. Rev.*, **141**, 1708–1730, https://doi.org/10.1175/MWR-D-12-00138.1.

Wang, C.-C., C.-Y. Kung, C.-S. Lee, and G. T.-J. Chen, 2012: Development and evaluation of mei-yu season quantitative precipitation forecasts in Taiwan river basins based on a conceptual climatology model. *Wea. Forecasting*, **27**, 586–607, https://doi.org/10.1175/WAF-D-11-00098.1.

——, M.-S. Li, C.-S. Chang, P.-Y. Chuang, S.-H. Chen, and K. Tsuboki, 2021: Ensemble-based sensitivity analysis and predictability of an extreme rainfall event over northern Taiwan in the Mei-Yu season: The 2 June 2017 case. *Atmos. Res.*, **259**, 105684, https://doi.org/10.1016/j.atmosres.2021.105684.

——, T.-Y. Yeh, C.-S. Chang, M.-S. Li, K. Tsuboki, and C.-H. Liu, 2023: A modeling study of an extreme rainfall event along the northern coast of Taiwan on 2 June 2017. *Atmos. Chem. Phys.*, **23**, 501–521, https://doi.org/10.5194/acp-23-501-2023.

Yeh, H.-C., and Y.-L. Chen, 2003: Numerical simulations of the barrier jet over northwestern Taiwan during the mei-yu season. *Mon. Wea. Rev.*, **131**, 1396–1407, https://doi.org/10.1175/1520-0493(2003)131<1396:NSOTBJ>2.0.CO;2.

Yihui, D., and J. C. L. Chan, 2005: The East Asian summer monsoon: An overview. *Meteor. Atmos. Phys.*, **89**, 117–142, https://doi.org/10.1007/s00703-005-0125-z.

Zhang, F., M. Minamide, R. G. Nystrom, X. Chen, S.-J. Lin, and L. M. Harris, 2019: Improving Harvey forecasts with next-generation weather satellites: Advanced hurricane analysis and prediction with assimilation of *GOES-R* all-sky radiances. *Bull. Amer. Meteor. Soc.*, **100**, 1217–1222, https://doi.org/10.1175/BAMS-D-18-0149.1.

Zhang, M., K. L. Rasmussen, Z. Meng, and Y. Huang, 2022: Impacts of coastal terrain on warm-sector heavy-rain-producing MCSs in southern China. *Mon. Wea. Rev.*, **150**, 603–624, https://doi.org/10.1175/MWR-D-21-0190.1.

Zhang, Y., X. Chen, and M. M. Bell, 2023: Improving short-term QPF using geostationary satellite all-sky infrared radiances: Real-time ensemble data assimilation and forecast during the PRECIP 2020 and 2021 experiments. *Wea. Forecasting*, **38**, 591–609, https://doi.org/10.1175/WAF-D-22-0156.1.

Zhao, H., Y. Shu, Y. Mao, Y. Liu, and K. Yu, 2023: The assimilation effect of multi-new types observation data in the forecasts of meiyu-front rainstorm. *Atmosphere*, **14**, 693, https://doi.org/10.3390/atmos14040693.